Test Beam Measurements with the EUDET Pixel Telescope

J. Behr[*]

December 23, 2010

Abstract

Test-beam measurements were performed with the EUDET pixel telescope. During the work for this thesis[1], the online-monitoring software was improved, the Mimosa 26 sensors were integrated into the offline analysis software and the data taken with these sensors were analysed. The first data were taken with the demonstrator telescope together with three Mimosa 26 sensors that were operated as devices-under-test. The second data sample was taken with a telescope that consisted of six Mimosa 26 sensors, of which five could be used. The single-point resolution and the detection efficiency were determined and found to be consistent with the expectation.

[*]University of Hamburg, DESY
[1]This report was published as part of a PhD thesis (DESY-THESIS-2010-038).

Contents

1. Introduction

The next planned high-energy collider is a linear electron-positron collider – the "International Linear Collider" (ILC) [1] or the "Compact Linear Collider" (CLIC) [2] – operated at a centre-of-mass energy of about $500 - 1000$ GeV (ILC) or up-to 3 TeV (CLIC).

Crucial requirement in many physics analyses at the ILC will be the reconstruction of secondary vertices arising from the decay of (heavy) c- and b-quarks and τ-leptons [3] very close to the primary interaction point. Events with these topologies can be used e.g. for the measurement of quark charges or for tagging b-quarks in jets in order to discriminate events in which top quarks decayed from background processes [4].

The vertex detector [5] for the track and vertex reconstruction foreseen for the ILC must have a polar-angle coverage as hermetic as possible and the innermost layer has to be as close to the interaction point as possible. In order to reduce the impact of multiple scattering the layer thickness of the vertex detector – including cooling – has to be very thin ($0.1\% X_0$ per layer). It has to be capable to cope with the ILC bremsstrahlung background and the average power consumption has to be moderate in order to reduce the amount of cooling needed. The readout of the vertex-detector sensors must be adapted to the proposed bunch-crossing structure of the ILC. The sensors installed in the vertex detector must have a very high granularity in order to provide a spatial resolution of < 5 μm [6] obtained with pixel sensors with a pitch of < 20 μm.

At the moment, several different technologies are developed and investigated for the ILC vertex detector such as CCD [7], CMOS [8, 9] or DEPFET [10] sensors and others.

In order to support the research and development of such technologies, the EU-DET project, supported by the "European Union" in the "6th Framework Programme" (FP6), would like to enhance the available test-beam infrastructure. The subproject JRA1 is intended to provide a high-resolution pixel telescope that can be operated in a magnetic field of 1.2 T. It should be noted that this telescope is not restricted to developments and studies for the ILC.

It was decided to follow a two stage approach: First, a so-called "demonstrator telescope" was constructed quickly using well established analog sensors. This telescope was available already 18 month after the start of the project. Since these analog sensors have not matched the design requirements of the project, the telescope was upgraded with new sensors in late Summer 2009 in order to reach the final resolution and readout rate.

In this thesis, some of the required changes for the upgrade to the final telescope and the first analysis of data taken with the upgraded EUDET telescope are described and discussed. First, in chapter 2 the experimental setup is introduced and the analysed data samples are specified. In chapter 3 some of the adjustments to the data-acquisition software are described. After briefly describing the main parts of the

offline analysis-software in chapter 4, the results of the data analysis are presented in chapter 5 and finally summarised in chapter 6.

2. Experimental Setup

The EUDET telescope is designed to be used in a wide range of detector research and development studies. Therefore, the telescope has to provide a flexible and portable infrastructure in order to be able to investigate quite different devices-under-test (DUTs) with low-energetic electrons ($1 - 6$ GeV) at DESY as well as with high-energy (> 100 GeV) hadron beams at the SPS facility at CERN under varying beam conditions.

The telescope consists of two arms each equipped with three sensors kept at a stable temperature by a cooling system [11]. The positions of the sensors along the beam axis can be adapted to the respective requirements. Between the two arms an optional mechanical x-y-support stage that allows to position the DUT with a few micrometer precision is installed.
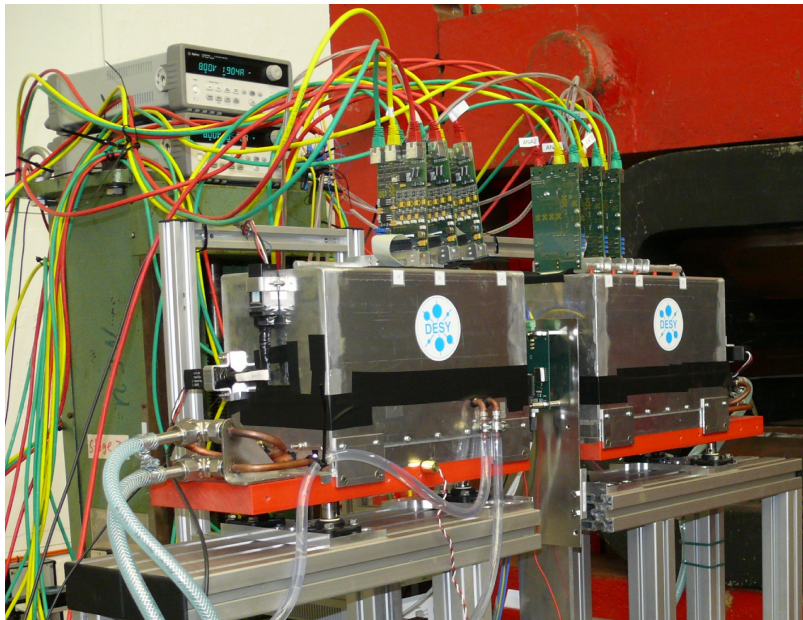
Figure 2.1: The telescope installed at DESY. A DUT [12] is installed in between the two boxes (figure taken from [13]).

A photograph of the EUDET telescope together with an installed DUT [12, 13] taken during a test-beam measurement at DESY is shown in figure 2.1. In this exemplary picture, the DUT is a high-voltage "Complementary Metal Oxide Semiconductor" (CMOS) monolithic detector placed in between the two telescope arms.

In figure 2.2 the hardware components of the telescope and their interconnections are illustrated. The sensors are read-out by dedicated data-reduction boards that transfer their data to a computer where the data-acquisition software is running. A trigger system including four scintillators connected to photomultiplier tubes allows to trigger on particles passing the telescope.

In this chapter, the main hardware components[1] of the telescope are described and

---

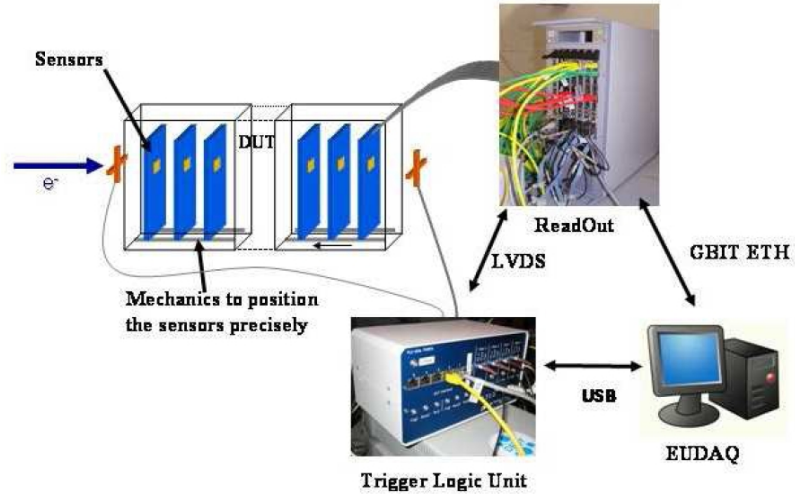[1]The data-acquisition system is discussed in chapter 3.

Figure 2.2: Schematic overview of the main telescope components (figure taken from [14]).

finally the analysed data sample is specified.

2.1. Hardware

In this section, the sensors, the readout hardware and the trigger system are described.

2.1.1. The Sensors

The sensors for the telescope have to provide a single-point resolution of $2-3$ μm with a minimum of material in order to reach a reasonably good telescope resolution even at lower beam energies of $1-6$ GeV where the contribution from multiple scattering becomes large.

At the time when the telescope concept was developed, the "Monolithic Active Pixel Sensors" (MAPS) [8, 15] technology was the only available vertex-detector technology[2] for future collider experiments that could provide ≈ 2cm^2 large sensors. In particular, the MIMOSA[3] detector series [9] successfully developed, fabricated and extensively studied at the CNRS-IPHC institute in Strasbourg, was utilsed for the telescope.
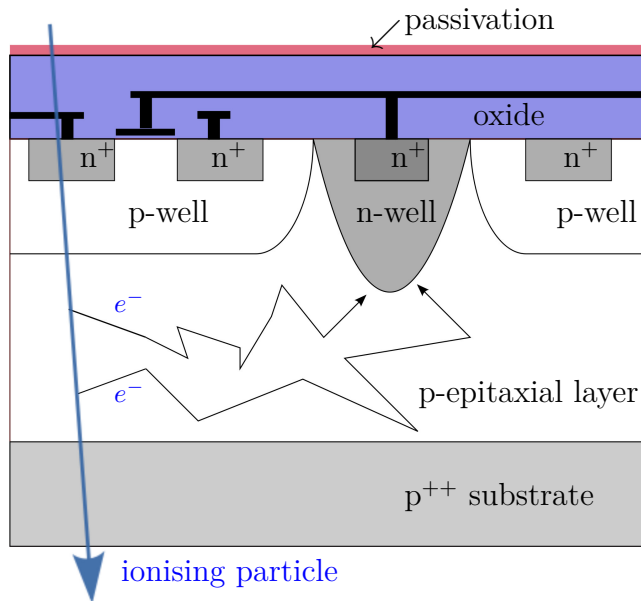
2.1.1.1. Monolithic Active Pixel Sensor

Monolithic CMOS detectors offer the possibility to integrate read-out circuits onto the sensors.

A cross section of a "Monolithic Active Pixel Sensor" is sketched in figure 2.3. The sensor is fabricated on a lightly-doped p-epitaxial layer grown on a highly-doped p^{++} substrate. The pixel readout circuit is embedded in a p-well on top of the epitaxial layer. The charge-collecting diode is formed by a junction between the n$^+$-doped implant and the p-epitaxial layer. Therefore, the sensor is only depleted directly underneath the charge-collecting n-well diode. Due to the large doping difference between the epitaxial layer and the p-well and the p^{++} substrate, respectively, potential barriers at

---

[2]A general-purpose overview of various pixel-detector technologies can be found in [16].

[3]MIMOSA stands for "Minimum Ionizing MOS Active Pixel Sensor".

Figure 2.3: Schematic cross section of a "Monolithic Active Pixel Sensor" (MAPS).

the boundaries are created. A passing ionising particles creates electron-hole pairs in the sensor material and those electrons produced in the epitaxial layer diffuse towards the charge-collecting n-well diode, where the electronic signal is measured. In the p^{++} substrate, usually made of "low quality" silicon, the recombination time of charge carriers is short compared to the corresponding time in the lightly-doped epitaxial layer.

Since the sensitive volume is placed directly underneath the electronics and the generated charge is kept in this volume by potential barriers, a "fill factor", which is the fraction of the pixel area that is sensitive, of 100% can be achieved.

The MAPS detectors have several additional advantages compared to other technologies: CMOS pixel detectors are potentially very cheap because standard cost-effective processing technologies can be used. Since the readout circuit in each pixel is only active during readout and due to the fact that no additional external bias voltage is applied, the power consumption is typically relatively small. Despite the small signal, sufficient signal-to-noise ratios can be obtained due to the very low input capacitances. The granularity of the pixel matrix is fine providing a good spatial resolution of a few micrometer for tracking detectors. Since the epitaxial layer is very thin ($< 20\ \mu$m) and the substrate can be thinned, the amount of multiple scattering of passing particles in the detector material can be limited. Owing to the thin epitaxial layer the positition resolution is also good for large incident angles.

The main disadvantages are the restriction to n-MOS transistors for the pixel circuit limiting the complexity of the integrated electronics and the sensitivity to radiation damage. Another disadvantage is in some environments the relatively large integration time compared to other technologies and the slower charge collection time.

2.1.1.2. Mimosa Sensors

The pixel sensors for the telescope have been fabricated using the AMS 0.35 OPTO process. On each pixel of the MAPS sensors utilised in the EUDET telescope a

so-called self-biased on-pixel amplifier [17, 18] is implemented. This mechanism clears the pixel signal and compensates for leakage current. The clearing process is slow compared to the readout frequency. Thus, the generated signal charge remains for several readout cycles in the pixel. The application of "Correlated Double Sampling" (CDS) avoids double counting of the signal by determining the difference of two or three successive read-out pixel signals. Owing to this approach an explicit reset of the pixel matrix is not nessesary.

The MIMOSA sensors typically provide a signal-to-noise ratio for minimum ionising particles (MIPs) of $20 - 40$ and a detection efficiency for MIPs depending on the thresholds of $> 99\%$.

The "demonstrator telescope" was equipped with MIMOTEL prototypes [19] with a pixel pitch of 30 μm in both directions providing an active area of 7.7×7.7 mm^2 that consists of a 256×256 pixel array. In addition, a high-resolution plane (MIMOSA 18) with a pixel pitch of 10 μm can be used at the expense of a slower readout rate. This high-resolution sensor consists of 512×512 pixel providing a sensitive area of $5 \cdot 5$ mm^2. Simulation studies [20] and test-beam measurements [21] have demonstrated that the usage of one of these high-resolution planes in the telescope can significantly improve the intrinsic telescope resolution. The readout time of the MIMOTEL (MIMOSA 18) sensors is 800 μs (3 ms) which is in this architecture equal to the time over which signals are integrated.

However, an integrated data-reduction architecture (e.g. CDS, zero suppression) on the sensor is missing for the two sensors described above. Therefore, these sensors do not fulfil the readout performance requirements of the final telescope.

In order to cope faster with the accumulated data an on-sensor CDS, an integrated zero suppression, and the possibility to provide a fully binary output was implemented in the MIMOSA 26 sensors [22, 23]. These sensors were in particular developed for the operation in the final EUDET telescope.

The MIMOSA 26 sensor is a combination of the MIMOSA 22 sensor [24] and the SUZE01 chip [25] that performs online data sparsification. The sensor is subdivided into 1152 columns of 576 pixels with a pitch of 18.4 μm providing a high granularity. The sensitive area of the sensors is approximately 21×10.6 mm^2.

On each pixel an amplification and CDS circuit is implemented. The sensor is read-out in a column-parallel mode with a pixel-readout frequency of 80 MHz which results in a integration time of about 112 μs. Each column is equipped with a discriminator that performs an offset compensation and a second column double sampling. Furthermore, the data are pipelined and sparsified by zero-suppression stages. The data sparsification allows a faster data throughput and due to the small integration time the hit multiplicity is reduced. A data compression factor of 10 to 1000 can be achieved [26].

In this analysis, the analog pixel signals were available in the data from the MIMOTEL sensors, while the pixel signals for the MIMOSA 26 data were purely binary.

2.1.2. The Data Reduction Boards

The pixel sensors were read-out by custom-made "EUDET Data Reduction Boards" (EUDRBs) [27, 28]. The EUDRBs were adapted to the readout of several different versions of MIMOSA sensors.

The operation of the EUDRBs is controlled by a "Field Programmable Gate Array" (FPGA). A mother/daughter-board approach was chosen in order to maximise the flexibility. The sensor specific components have been implemented on removable and interchangeable daughter cards, while on the motherboards the memory and computing elements were placed.

The EUDRBs perform CDS, pedestal subtraction and zero suppression with a configurable threshold. Owing to this approach the size of the transfered data can be reduced compared to a full-frame readout where all pixel signals are transferred without further data processing.

Each sensor is read-out by one EUDRB, while the data of the individual EU-DRBs are transfered through a VME bus to a VME CPU (PowerPC MVME6100) and from there via Ethernet to the data-acquisition software (chapter 3 for more details). Detectors with JTAG programmable features can be configured with the EUDRBs as well. One EUDRB has to be configured as timing master and must be connected to the trigger system (chapter 2.1.3). This timing master distributes the trigger signal to the other EUDRBs.

Furthermore, the sensors can be read-out either asynchronously or synchronously. While the first readout was typically used for the demonstrator telescope equipped with either MIMOTEL or MIMOSA 18 sensors, the latter was used for the readout of the final telescope. The MIMOTEL telescope was read-out asynchronously because a higher noise level was observed when running synchronously [29].

2.1.3. The Trigger Logic Unit

In order to provide a simple and easy to use trigger system, a dedicated "Trigger Logic Unit" (TLU) [30–34] was developed in the EUDET JRA1 project. The TLU was designed to be as flexible as possible whilst only few restrictions on the user of the TLU were introduced.

The dedicated trigger system is based on an USB programmable FPGA board and it provides coaxial connector interfaces that accept NIM, TTL or photo-multiplier level pulses for the generation of a beam-trigger. In addition to the beam-trigger, the TLU can be run in a self-triggered mode as well. The trigger signal is distributed via RJ45 and/or LEMO connectors to the connected DUTs.

Several handshake modes are available for the communication between the connected hardware and the TLU: 1) Without handshake the TLU is not interpreting busy signals from the DUTs; the trigger line is set for a fixed length of time. 2) In contrast, in the trigger-handshake mode the trigger line is set and the connected DUTs raise the busy signal until they are available for new trigger signals. 3) The trigger/data-handshake mode is similar to the trigger-handshake mode. In addition, the connected DUTs can read-out the trigger number while holding the busy signal. The

latter is used for the connection of the EUDRBs to the trigger system and it's the recommended method for the DUT integration.

2.2. The Data Samples

The data studied in this analysis were taken with the EUDET pixel telescope mounted at the H6 beam line at the SPS facility at CERN. The beam line was configured to provide 120 GeV hadrons. The beam size was approximately ≈ 3 cm (FWHM) and the beam intensity has been tuned such that about one particle per readout cycle was observed. Two slightly different experimental setups were used:

- **July 2009 Test Beam:** The goal of this test-beam measurement was the integration of the MIMOSA 26 sensors into the available telescope data-acquisition system and the analysis of the combined data. Therefore, three of these sensors were integrated as DUT layers into the telescope, whereas for the telescope MIMOTEL sensors were used. The integration was done such that the three MIMOSA 26 were read-out with three EUDRBs integrated in one VME crate. With this approach the performance of the sensors for the final telescope could be studied before the final upgrade of the whole telescope.
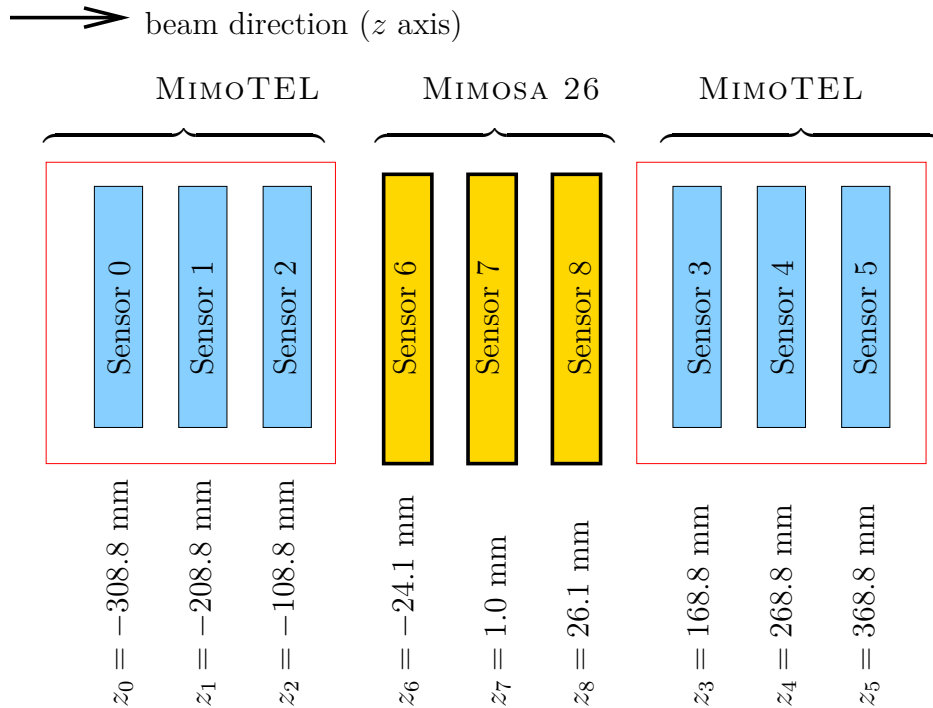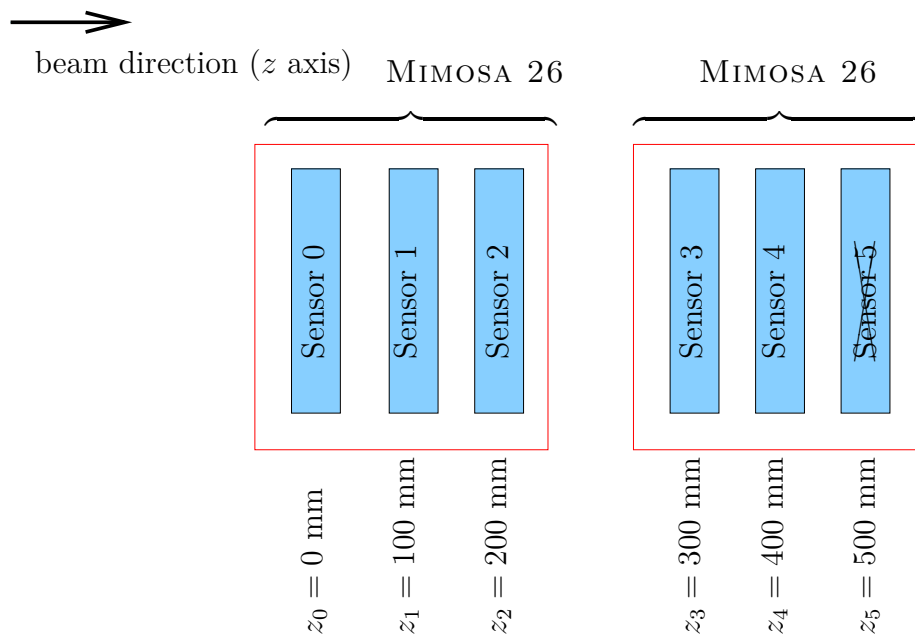

Figure 2.4: The experimental setup for the July 2009 test-beam measurement. Three MIMOSA 26 sensors were treated as DUTs.

Figure 2.4 illustrates the experimental setup of this test-beam measurement schematically. The MIMOSA 26 sensors were configured with a signal-to-noise threshold setting of $S/N > 12$ in order to reduce the fake rate coming from

noise hits in the first data. The analysed data sample consisted of approximately 100000 events with an average track multiplicity of 1.

- **September 2009 Test Beam:** During September 2009, the six Mimo-TEL telescope sensors were replaced by Mimosa 26 sensors. These sensors were read-out with in total six EUDRBs, while always three of them were integrated in one VME crate in order to avoid VME-bus throughput limitations. One of the sensors (sensor 5) could not be used due to an electrical connection problem.

Figure 2.5: The experimental setup for the September 2009 test-beam measurement. Sensor 5 was not used.

During the data taking a data-taking peak rate of approximately 990 Hz was achieved. In contrast to the July data taking, the sensors were configured with a lower signal-to-noise threshold of $S/N > 10$ in order to improve the resolution and detection efficiency. The analysed data sample consisted of approximately 1.5 million events with about $1 - 2$ tracks per event.

Since the system was rather new, the higher threshold settings were used as mentioned above. Today, the telescope sensors are configured with thresholds of $S/N > 8$ or even $S/N > 6$.

3. The Data Acquisition Software

The EUDET pixel telescope has a flexible data-acquisition software (EUDAQ) [35–37] that was designed to be modular and portable. The software makes use of several individual independent programs (producer) that are connected with each other over the network as shown in figure 3.1. The hardware of the telescope and of the possibly connected DUTs is read-out by separate producer tasks that are connected to the "run control" and to the "data collector". The latter receives the data streams, builds the events and stores the data on the storage device. The "log collector" provides an interface for the producers for the collection of logging messages. One part of the EUDAQ software is the online-monitoring system (RootMonitor) that makes use of the object-oriented data analysis framework ROOT [38] implemented in C++. The RootMonitor was successfully tested and used during past test-beam campaigns of the telescope at DESY and at CERN.

During the work for this thesis, the usability and performance of the RootMonitor was improved. Therefore, in this chapter an overview of some of the RootMonitor developments is given.
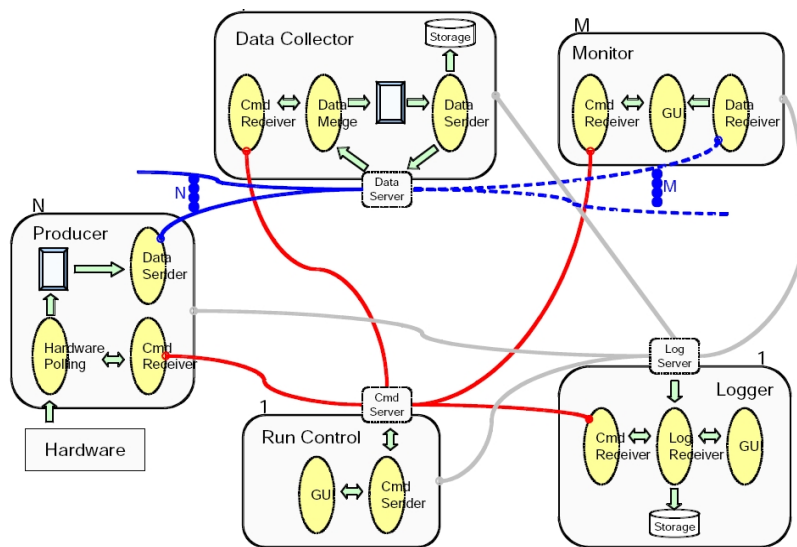
Figure 3.1: The schematic layout of the EUDAQ software. Several individual producer tasks are connected over the network (figure taken from [39]).

3.1. Event Reconstruction

Several reconstruction algorithms are used for the event reconstruction in order to monitor the data quality.

The RootMonitor can be used together with the EUDAQ system during data taking as well as a stand-alone application reading and analysing raw data files.

The RootMonitor is able to handle different sensor types for the various telescope planes. The sensor types must be specified in a dedicated configuration file. The

reconstruction algorithms account for different sensors types automatically. It is also possible to specify an additional file that contains for the DUT the pedestal and noise values.

In order to roughly estimate the noise of the MimoTEL or Mimosa 18 sensors, the root mean squares of the signal values are determined. This information is used in the cluster-reconstruction algorithm. The signal values are calculated with the application of a correlated double-sampling method (CDS) as provided by the EUDAQ library. In addition, every 50. events a combined CDS distribution for each sensor plane is determined and the noise for the corresponding sensor is extracted (section 3.2.1).

3.1.1. Cluster Reconstruction

The RootMonitor provides a simple fixed-frame cluster-reconstruction algorithm e.g. for MimoTEL sensors. Seed pixel candidates are identified and starting from the pixel with the highest signal-to-noise ratio clusters are constructed by joining neighbouring pixel to the cluster if certain thresholds are fulfilled. In this analysis, the possibility to adjust these thresholds in the graphical user interface was implemented. In addition, the algorithm was generalised in order to cope with different cluster sizes – 3×3 and 5×5.

In this analysis, for the Mimosa 26 sensors an additional cluster algorithm was implemented. This algorithm starts from one hit candidate and then assigns all 8 neighbouring hit pixels to the cluster. This procedure is repeated until all hit pixel are joined into clusters. In order to reduce the impact of noisy pixels, an algorithm that identifies these pixels stores the information for all hit pixels and if for 200 events the pixel fired in more than 15% of the events such pixels are marked as noisy. This threshold was roughly tuned by using the data from a sensors that had a known structure of bad pixels.

Moreover, two different methods for the cluster-position reconstruction are available in the RootMonitor. Either the position of the seed pixel is used or the centre-of-gravity for each cluster is determined. The latter is a signal-weighted average of the pixel positions belonging to the cluster.

3.2. The Graphical User Interface

In this section the graphical user interface (GUI) of the RootMonitor is described and some of the available histograms. These histograms are intended for the control of the data quality during data taking.

3.2.1. Available Histograms

Some of the important histograms are described in the following:

- **Time Dependence of Noise:** As previously described, the time dependence of the noise is monitored. This is in particular interesting for the monitoring of the telescope cooling. This information is only available if the telescope runs in raw mode and if the telescope sensor planes are MimoTEL or Mimosa

18 sensors. Figure 3.2 shows the time dependence of the noise in ADC counts, which is in this case almost constant. The different sensor planes are indicated with different colours.
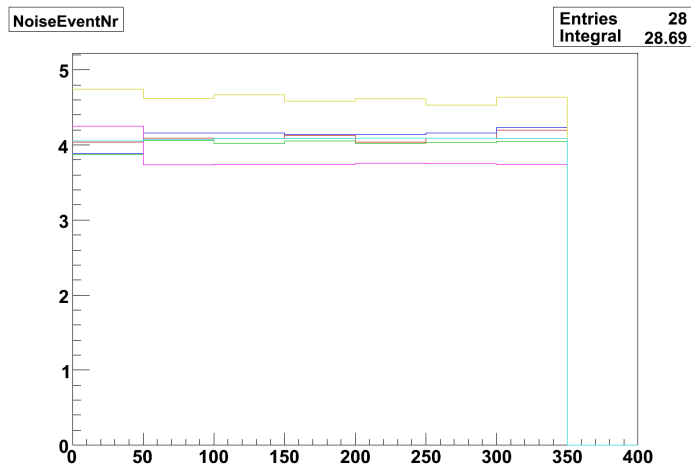
**Figure 3.2**: The noise for each sensor plane as a function of time (event number) in ADC counts.

- **Cluster Correlations:** During the assembly of the experimental setup it is typically difficult to position the telescope inside the beam. In order to allow an easier positioning correlation plots were implemented in the ROOTMONITOR.

  Beam particles passing the telescope planes create clusters in the sensors. These clusters are spatially correlated between the individual planes. Therefore, for neighbouring sensors the reconstructed position in x and y direction for all possible pairs of cluster was filled into 2-dimensional histograms. Correlations can be identified as straight lines in these histograms.

  As an example, figure 3.3 depicts the x and y correlation plots for pairs of neighbouring planes as well as the correlation between the first and the last plane. Deviations from a diagonal line can be interpreted as telescope misalignment. In this example, the orientation of the sensors in the second arm differs from the orientation in the first arm. Thus, the slope of the line is not the same in all histograms. Additionally, the sensor 3 has a smaller pixel pitch.

  In the case of a DUT the ROOTMONITOR is able to provide correlation plots that show the cluster position correlation between the DUT and the telescope. This can be seen in figure 3.4 where, as an example, correlations between the telescope planes and a DEPFET sensor [40] are depicted.

  Previously, the correlation of cluster positions in different sensor planes was described. These histograms are only helpful if the influence of multiple scattering is sufficiently small and if the multiplicity is low.

  In order to provide additional correlation histograms the correlation between the number of reconstructed hits in the sensor planes was implemented in the ROOTMONITOR. Figure 3.5 illustrates the correlation that can be observed as a cloud following a diagonal line. In this example, the offset in some of the plots is caused by the different amount of sensor noise. The number of bins can be adjusted via the GUI in order to match to the data multiplicity.

13
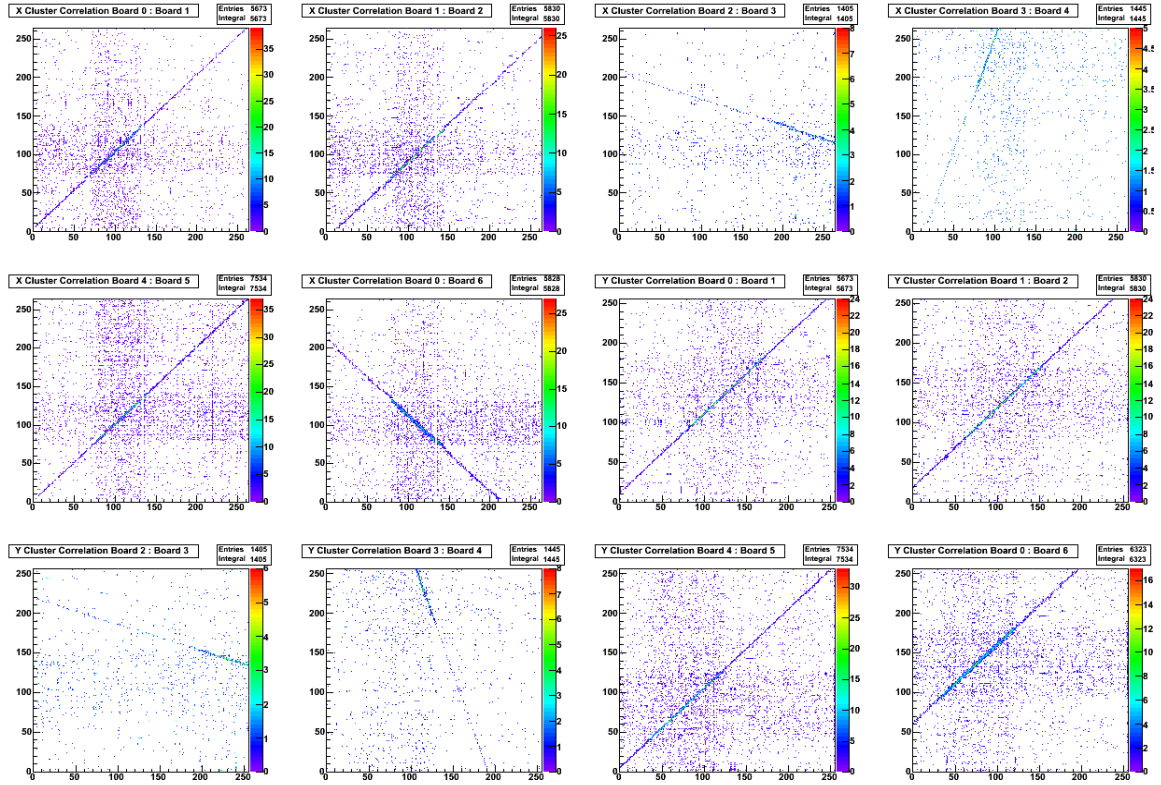
Figure 3.3: Cluster position correlation between pairs of sensor planes. In this example, sensor no. 3 has a smaller pixel pitch.

- **CDS Lego:** The "CDS Lego" plots were implemented in order to observe particle hits on an event-by-event basis. Every N^{th} event the corresponding plots for all sensor plane are filled with the current signal values. The variable N can be adjusted in the GUI.

  Figure 3.6 shows as an example CDS values for two sensors for event number 40 where one hit can be seen.

3.2.2. Configuration Menu

Sometimes it is necessary to change reconstruction parameters online without modifying the source code of the RootMonitor. In order to ensure a better usability, the possibility to change online via the GUI parameters was implemented.

In figure 3.7 a screen shot of the configuration tab is depicted. In this menu several parameters can be adjusted. On the right-hand side a list of check boxes is provided. These check boxes can be used in order to enable or disable pads of histograms. The check boxes are grouped into three parts depending on where the corresponding histograms are shown. After pushing the "Apply" button the configuration is updated and all canvasses are divided dynamically depending on the number of active pads. Histograms belonging to disabled pads are filled in the background. Thus, the information is not lost. If currently not needed pads are disabled, then the performance of the RootMonitor GUI increases. Furthermore, the number of enabled pads
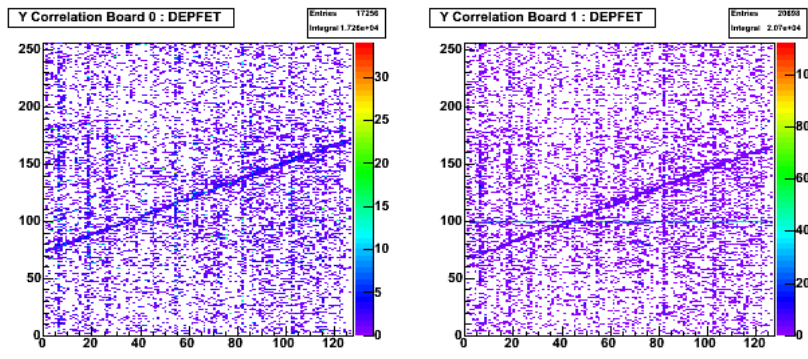
Figure 3.4: Examples for cluster position correlations between telescope sensors and a DEPFET sensor operating as DUT.
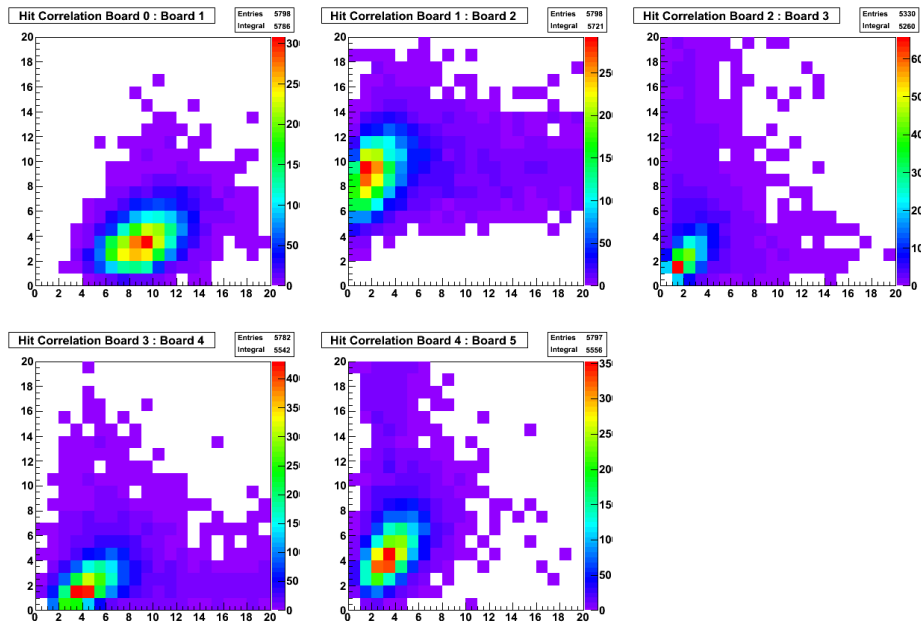

Figure 3.5: Correlation between the number of hits in neighbouring telescope planes.

is counted, the canvasses are then suitably divided and the stacks of histograms are drawn using the corresponding drawing options. It is also possible to refresh the histogram view.

In the window header the current file name, the run and event numbers are depicted. It is possible to reduce the number of processed events and change the time interval after which the RootMonitor is forced to update the histogram drawings.
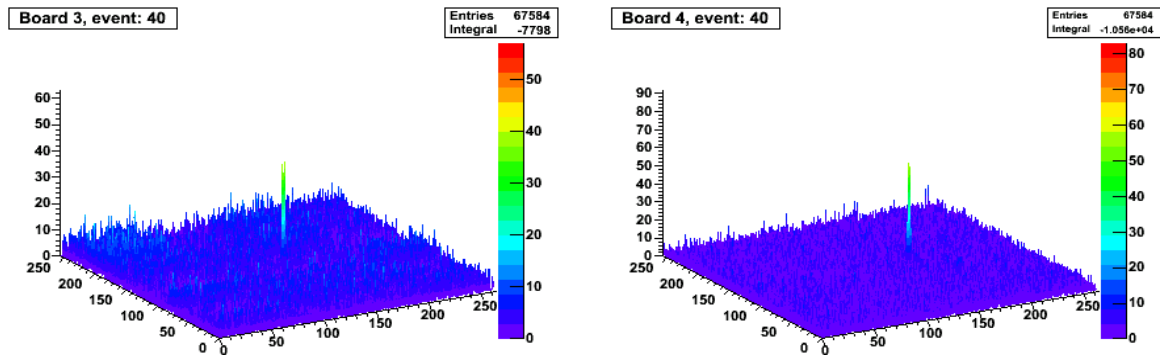
Figure 3.6: The CDS value for sensor plane number 3 and 4 and event number 40.
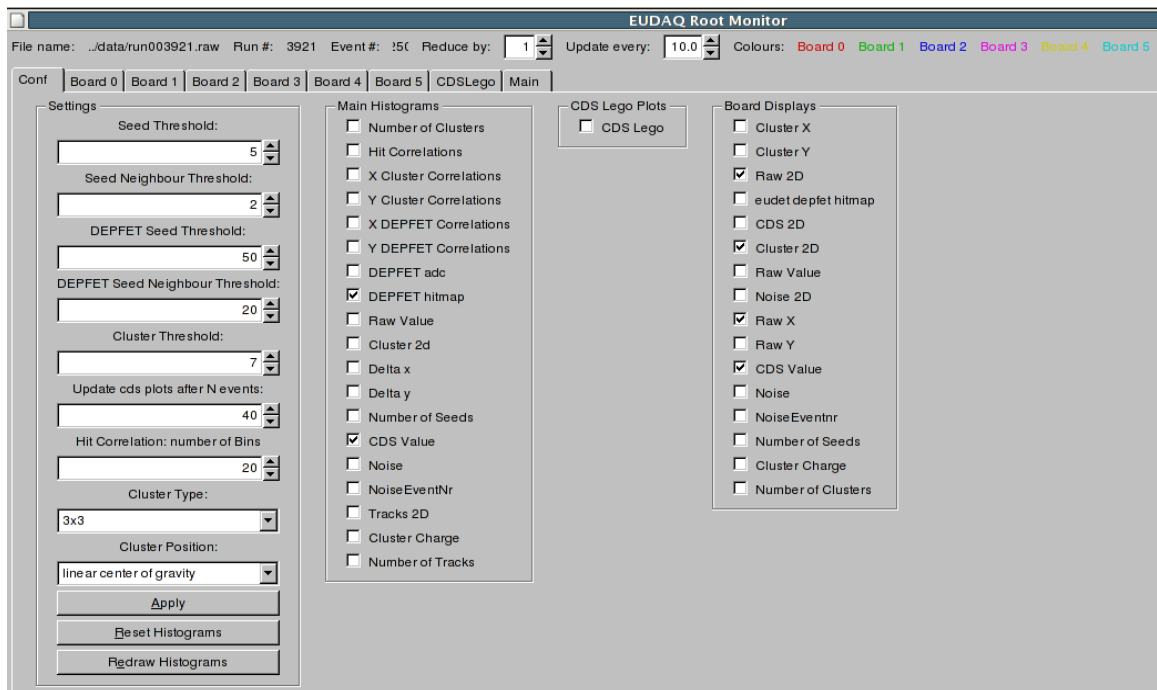

Figure 3.7: The configuration menu, where one can change online reconstruction parameters. It is also possible to enable or disable pads of histograms.

4. The Offline Analysis Software

The offline analysis software (EUTelescope) [41, 42] for the telescope data is based on Marlin [43–45] and LCIO [46, 47]. Even though EUTelescope was primarily developed for the analysis of the telescope data, it can also be adopted to the analysis of other data sets.

The EUTelescope software makes use of the Marlin analysis framework which divides the analysis in several individual small tasks – called "processors". The behaviour of these processors can be controlled with XML steering files. The data are stored in the LCIO format which was developed to provide a persistency data model and interface. The data are grouped into so-called "collections". Typically a Marlin processor takes as input several data or database collections, analyses the input collections, creates several histograms and produces potentially an output collection that can be either stored on the disk or used as an input for other processors. It is possible to perform each analysis step separately as well as the full chain at once.
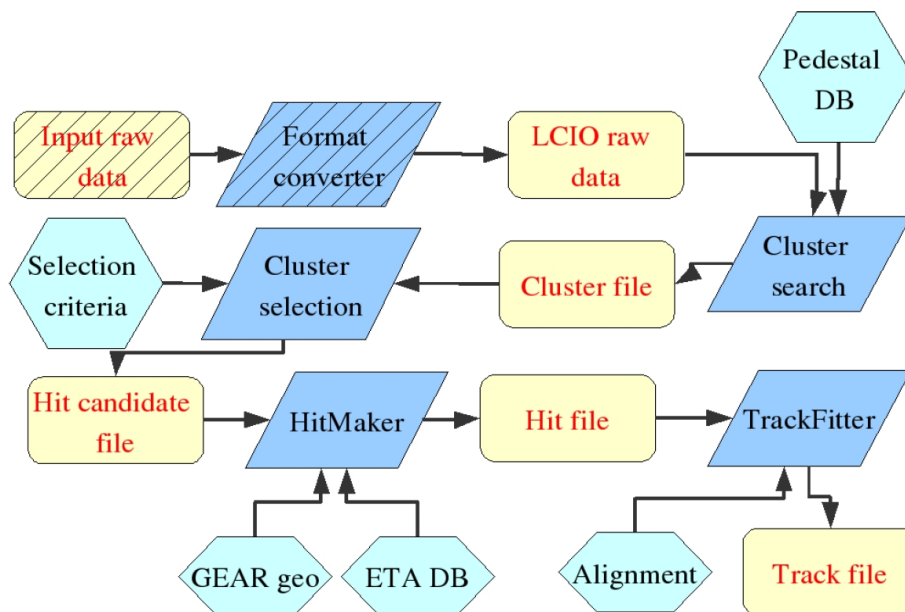
Figure 4.1: The schematic layout of the EUTelescope software (figure taken from [41]).

Figure 3.1 shows the schematic layout of the EUTelescope analysis chain. The first step of the data analysis is the conversion of the raw data files into the LCIO format. In general, this conversion is performed by making use of the corresponding functionality provided by the EUDAQ software[1], but it can be extended to convert

---

[1]A detailed description how the conversion has to be done in the EUDAQ library can be found in [37].

any other data set. After the conversion, depending on the data type and the requirements, pedestal and noise information are determined and hit pixels are grouped into clusters by applying loose selection and quality cuts. This collection of cluster candidates can be used in conjunction with an additional processor that applies some filtering criteria to obtain a collection of filtered clusters. Afterwards, the cluster coordinates are transformed from the local reference frame to the global telescope reference frame using the geometry description provided by the GEAR [48] package. After determining the alignment constants of the individual planes, the fitter reconstructs tracks using this collection of corrected hits. These tracks can be used for an extrapolation to the DUT surface in order to determine the predicted positions of hits in the DUT plane.

During the work for this thesis, the new MIMOSA 26 sensors were fully integrated into EUTELESCOPE. In order to implement these sensors in the software, several processors and algorithms had to be adapted to the different data format. In the following, some of the major changes needed for the analysis of data taken with these new sensors are briefly discussed.

4.1. Clustering

One of the first steps in the data analysis is the search for cluster candidates. The EU-TELESCOPE software provides several different algorithms like the "fixed frame clustering" that merges all neighbouring hit pixel that fulfil certain criteria to a cluster candidate. The size of these cluster can be specified in the steering file. Contrary to this algorithm the "sparse clustering" is not based on a fixed size and shape of the cluster. It utilises the distance between the pixel and the seed pixel[2] for the clustering. Therefore, these cluster mostly do not have a regular shape or size.

All the provided clustering algorithms use data collections that provide for each pixel the signal in ADC counts and the noise information. Since the new MIMOSA 26 sensors only provide binary information and no noise information, a new algorithm had to be developed – the "digital fixed frame algorithm".

In the EUTELESCOPE software package each cluster type is implemented as an individual C++ class. Since all cluster types have to provide the same functionality in order to be usable in the analysis framework, a generic abstract base class (EUTELVIRTUALCLUSTER) with several general virtual methods is implemented in the software. The classes for different cluster types inherit from this abstract class and all the virtual member methods are overridden with the necessary implementations.

The required changes needed for the MIMOSA 26 sensors were implemented by introducing an additional cluster type – called "EUTELDFFCLUSTER". This new cluster type provides all necessary member functions – for instance methods like the centre-of-gravity shift – in order to be fully operational in the analysis framework. The corresponding "digital fixed frame algorithm" creating these digital clusters is briefly described in the following:

---

[2]The seed pixel is defined as the pixel with the highest signal-to-noise ratio of the cluster.

- For all hit pixels the number of neighbouring hit pixels, N, is determined, whereas diagonal neighbours are ignored.
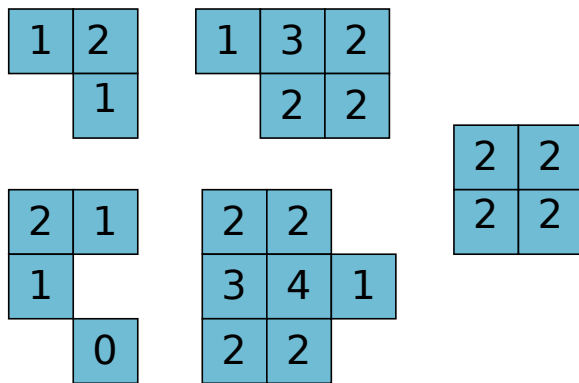
Figure 4.2: The "digital fixed frame algorithm": As examples five different cluster are shown. The indicated numbers represent the number of neighbouring pixel (ignoring diagonal neighbours).

Figure 4.2 illustrates as examples five cluster. The indicated numbers indicate the number of neighbours. The pixel with the largest N in a group of pixel is more likely to be the seed pixel than those pixel with smaller N. In case of symmetric clusters with more seed candidates the pixel that is read-out first is taken as seed.

- The list of hit pixel obtained in the previous step is sorted with decreasing N in order to determine the seed candidates. For pairs of pixel with equal N, the pixel with the larger number of diagonal neighbours is preferred.

- The resulting list is processed starting from the seed candidate with the greatest N.

- All hit pixel in a fixed $x \times y$ frame around the seed pixel are merged into the cluster and removed from the pixel collection and from the list of seed candidates. The size of the cluster can be specified in the corresponding steering file.

- Additionally, it is possible to reject all cluster that do not exceed a certain amount of hit pixel. By default this cut is disabled and was not used at all in the analysis presented here.

The described algorithm was fully integrated into EUTELESCOPE and it can be used not only for MIMOSA 26 data but also for other data.

4.2. Alignment

In order to be able to reconstruct tracks with the telescope and to extrapolate these tracks to the DUT plane, the geometrical positions of the sensor planes have to be known with a precision which is significantly better than the resolution. The EUTELESCOPE software packages provides a processor (EUTELMILLE) that uses MILLEPEDE [49, 50] for the determination of the alignment constants in order to reduce the bias and the uncertainty of the fitted track parameters and to minimize the χ^2 of the tracks.

Each parametrisation of a track depends on local parameters that vary between the tracks and on global parameters – the alignment constants. The processor EU-TELMILLE takes as an input a collection of hits and then for all combination of hits straight lines are fitted to these groups of hits independently in x and y direction. In order to suppress fake tracks resulting from combinatoric background, cuts on the residual distributions for all sensor planes can be specified in the corresponding steering file. The derivatives of the tracks with respect to all local and global parameters are stored in a binary file that can be read by MILLEPEDE. The MILLEPEDE software determines in a simultaneous linear-least-squares fit of all local and global track parameters the alignment constants for the sensor planes. Determined are shifts in x and y direction and rotations around the z direction. Usually the alignment constants of the first and the last plane are fixed in this determination in order to define the coordinate system and to obtain a stable fit result.

Since the number of planes that could be aligned with this software package was fixed to six and only planes belonging to the telescope were considered in this processor, some improvements of the EUTELMILLE processor had to be implemented:

- The EUTELMILLE processor was adjusted such that it can handle an arbitrary number of planes. All related cuts and steering parameters were adjusted accordingly.

- The possibility was implemented to use hits stored in several individual collections. The EUTELMILLE processor merges all hits from the individual collections together and performs the alignment for all planes simultaneously. This implementation together with the previously described modification enables EUTELMILLE also for the alignment of the DUT.

- Additionally, the possibility to use a combination of a hit and a track collection for the alignment of the DUT was implemented. The track collection can be created for instance with the analytical track fitter (see section 5.1.4 for more details) after aligning the telescope planes. These tracks can be exploited in the alignment processor in order to determine the alignment constants of the DUT. In this case, the alignment constants of the telescope typically have to be fixed in the fitting procedure.

After the implementation of these modifications the alignment package was suited for the data analysed for this thesis, where up-to nine sensor planes were used.

During the analysis of the MIMOSA 26 data a distinct residual structure, as shown in figure 4.3a, was observed when using the alignment processor. In order to investigate this structure, a very simple "toy" Monte Carlo study was performed. In this Monte Carlo approach five sensor planes were arbitrarily misaligned – ignoring rotations. Afterwards, particles were generated with a small beam spread and hits were created in the five telescope planes. The influence of multiple scattering was neglected. Since the MIMOSA 26 sensors provide binary data, the hit information was digitized using a pixel pitch of 18.4 μm. A detection efficiency of 95% per plane was assumed. Straight-line tracks were fitted to all combinations of hits and filled into residual histograms. The result of this study is depicted in figure 4.3b. It can be noted that
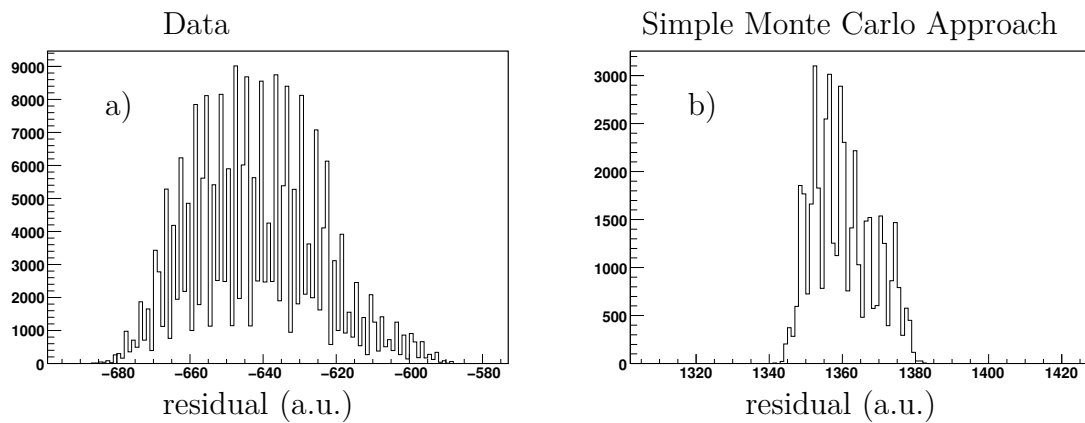
Figure 4.3: Residual between the measured hit position and the predicted hit position in the central sensor plane for a) data and b) a simple Monte Carlo model.

the general structure of the observed data residuals can be reproduced, whereas the details differ between the data and the Monte Carlo approach. Presumably, this disagreement is caused by an oversimplified Monte Carlo model. The spiky structure of the residuals is more pronounced for smaller beam spreads and for sensors in the central part of the telescope. This behaviour was also observed in the data.

5. Results

In this chapter, the analysis results for the data (chapter 2.2 for more details) taken in July and September 2009 at the SPS facility at CERN is presented and discussed. Both data samples were taken with a beam of 120 GeV hadrons.

5.1. July 2009 Test Beam

During the July 2009 test beam three MIMOSA 26 sensors were operated as DUTs in the telescope. A signal-to-noise threshold of $S/N > 12$ was applied to the MIMOSA 26 sensors. The telescope consisted of six MIMOTEL sensors.

5.1.1. Pedestal and Noise

During the data taking several dedicated small data samples for the determination of the pedestal and noise values of the MIMOTEL sensors were taken. For these data samples the EUDRBs were configured to provide the information for the full sensor matrices without applying any online zero suppression. The particle beam was turned off and the sensors were read-out with a fixed frequency. The pedestal value for every pixel separately was determined with the corresponding EUTELESCOPE processor by calculating the average signal in every pixel – rejecting the largest upward and downward fluctuations. The noise was defined as the root mean square (RMS) of the pedestal fluctuation.

Figure 5.1 shows two-dimensional histograms of the noise and pedestal values for sensor 3 as well as the distribution of these quantities. Except for the last sub-matrix of the sensor, the noise was determined to be around 3 ADCs, whereas the pedestal was found to be very close to zero. The reason is that the pixels are self-biased (section 2.1.1.2). The higher noise values in the last sub-matrix were caused by the read-out system and not by the sensors itself.

After the determination of the pedestal and noise values and after marking dead and noisy pixels this information was loaded into the EUDRBs. Afterwards, the EU-DRBs applied a zero-suppression algorithm online during the data taking. Only the signals of those pixel were not suppressed that have exceed a signal-to-noise ratio of 2. Additionally, the signals of pixels inside a 5×5 area around these pixel were included in the data stream from the EUDRBs.

In the offline analysis, the pedestal values were subtracted from the signal and the signals were corrected for common-mode shifts.

5.1.2. Cluster Reconstruction

As described in the previous chapter 4.1, clusters were reconstructed in the reference-telescope sensors (the analog sensors) with the application of the "fixed frame clustering"
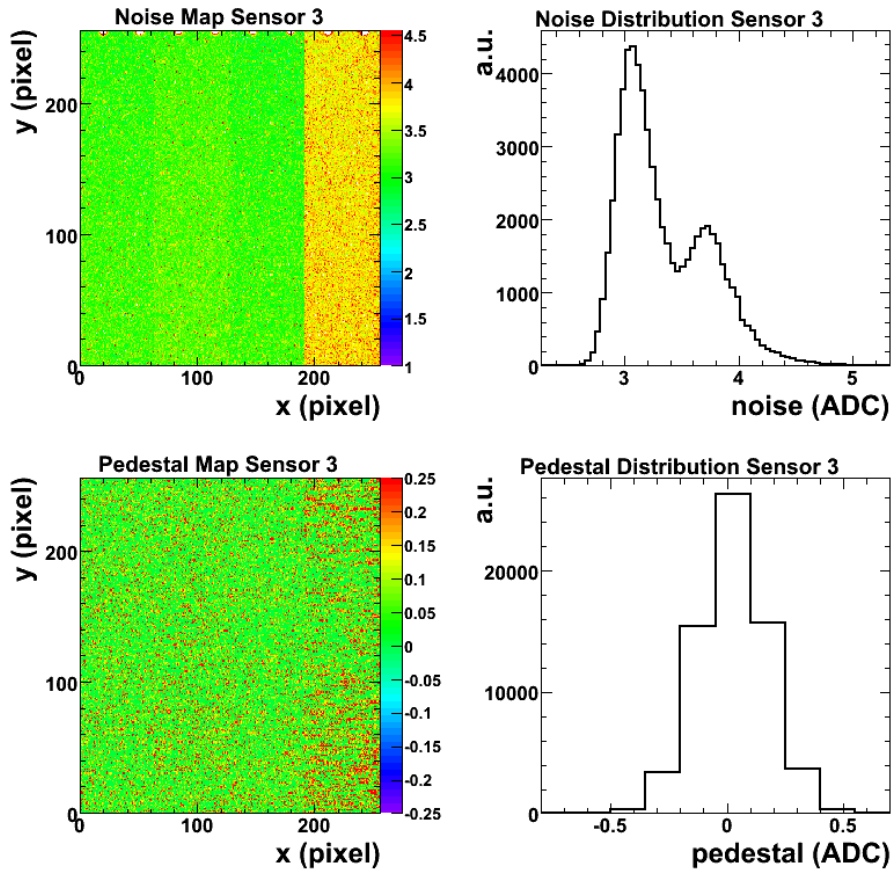
Figure 5.1: As an example the noise and pedestal values for sensor 3.

algorithm. For each sensor, cuts on the seed and cluster signal-to-noise ratios were applied in order to suppress noise. These cut values were adapted for each sensor separately as indicated in figure 5.2, where the seed signal-to-noise distribution before the application of cuts is depicted for sensor 2. The vertical lines illustrate the applied cuts. The peak on the left-hand side of the distribution below the indicated cut is the contribution from noise, whereas the peak on the right-hand side is related to the signals of particles.

For the reference telescope, cluster-signal distributions for parts of the data are presented in figure 5.3 after applying signal-to-noise cuts. Shown are also the fit results of Landau distributions[1] to the data. The data show reasonable cluster-signal spectra even though the fit does not agree perfectly with the data. It should be noted that during the data taking, an increasing detector noise was observed possibly caused by a non-constant temperature of the cooling water.

In contrast to the reference sensors, the "digital fixed frame algorithm" was used for the MIMOSA 26 (the DUT) data.

---

[1]Landau distributions describe the fluctuations in the energy loss of charged particles in thin layers of material.
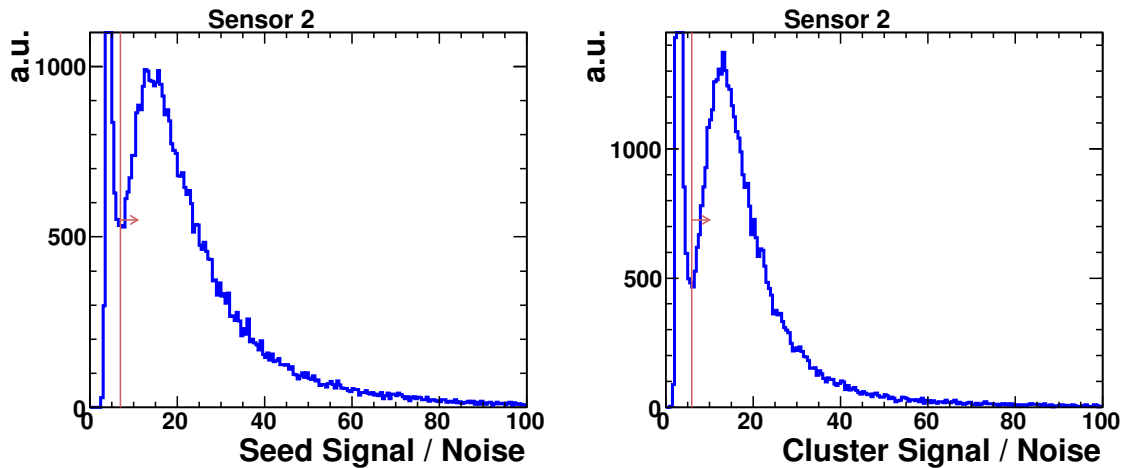
Figure 5.2: The seed and cluster signal-to-noise ratios. The vertical line indicates the applied cut values.

5.1.3. The η-Algorithm

The η-algorithm is a widely used standard method for the correction of non-linear charge-collection effects. The algorithm utilises the centre-of-gravity (CoG) shift within the seed pixel of clusters. These shifts should be uniformly distributed over the whole seed-pixel area, because the particle impact position inside the seed pixel is uniformly distributed.

The η correction discussed here was only applied to the data of the reference telescope and not to the binary MIMOSA 26 data, because with the applied threshold settings these data mainly consisted of single-pixel cluster. Therefore, a more detailed investigation of this correction with the new sensors was not possible.

Figure 5.4a shows for a small subset of the data the CoG shift separately in x and y direction. The η-algorithm integrates these distributions and the obtained function is normalised to the highest value and shifted by -0.5 as depicted in figure 5.4b, where η is shown as a function of the CoG shift. The discrete step at CoG equal to 0 is caused by the occurrence of single-pixel cluster. Figure 5.4c (5.4d) presents the correlation between the CoG shift in x and y direction before (after) the application of the η correction. The corrected distributions are much more uniform than the uncorrected ones.

In figure 5.5 the distribution of reconstructed hits on one of the MIMOSA 26 sensors is illustrated. The rectangular area with a higher density of hits is related to the trigger window (the geometrical overlap of the four used scintillators).

### 5.1.4. Alignment and Track Reconstruction

After transforming the cluster coordinates from the local reference frame to the global reference frame of the telescope, the alignment constants of the telescope planes and the three MIMOSA 26 sensors were determined with an approach that consisted of two iterations:
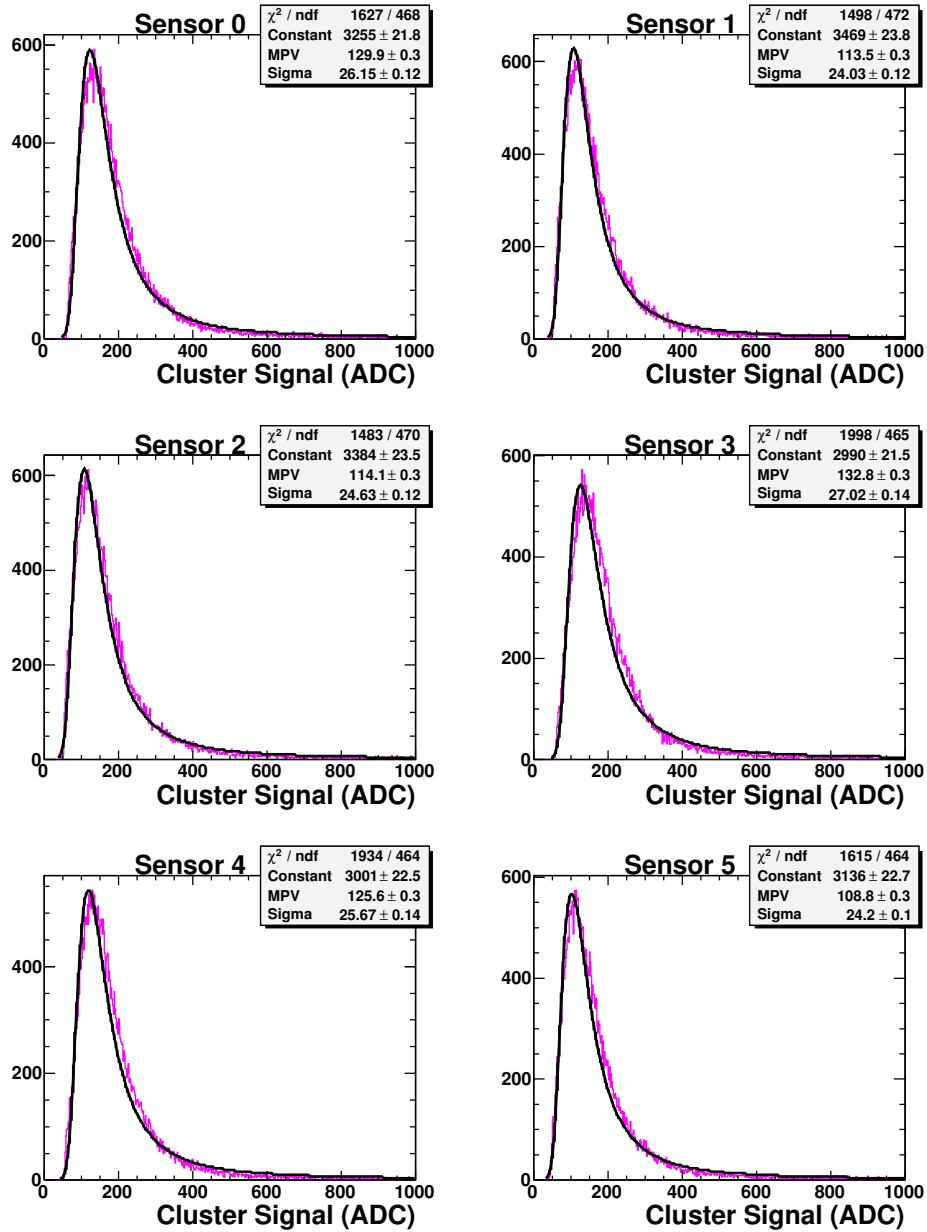
Figure 5.3: The cluster signal after applying cuts on the seed and cluster signal-to-noise ratios.

1. Only the telescope planes were aligned – the three DUT sensors were excluded from the alignment.

2. The alignment corrections were applied to the telescope planes and these planes were fixed in the fit. Afterwards, the three DUT sensors were included in the alignment procedure and their constants were extracted.

The procedure described above was repeated once in order to improve the alignment, because small rotational misalignments were observed.
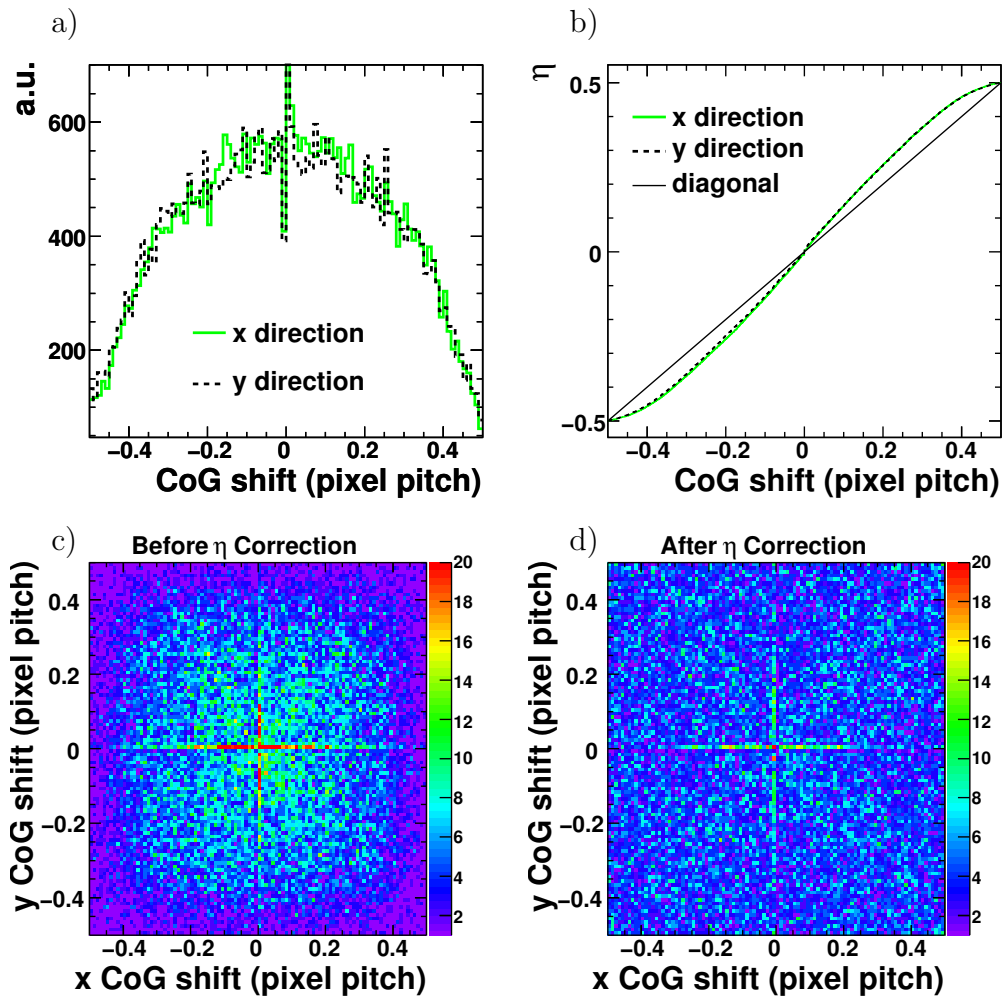
Figure 5.4: a) The centre-of-gravity (CoG) shift distribution in x and y direction. b) The η-function in x and y direction. c) Correlation between the CoG shift in x and y direction before applying the η correction. d) CoG shift correlation after applying the η correction.

Owing to the used approach the alignment of the telescope was performed independently from the DUT alignment. For the telescope planes typical sizes of the alignment corrections were < 0.5 mm for shifts in x and y direction and a few millirad for the rotation around the z axis. Since the positioning of the DUT in the telescope acceptance region is typically more difficult, the alignment constants for the DUTs were found to be significantly larger – about 4 mm (1 mm) for shifts in x (y) direction.

The algorithm for the track reconstruction utilised in this analysis makes use of an analytical track-finding approach [20] as provided by the EUTELESCOPE software. This algorithm takes into account the multiple scattering of particles in the detector material in the definition of the corresponding χ^2 function. The algorithm assumes that the scattering angles of the particles are small, that the sensor planes are parallel to each other, that the beam has only a small angular spread, that the beam is perpendicular to the telescope planes, that the energy loss of particles in the sensor
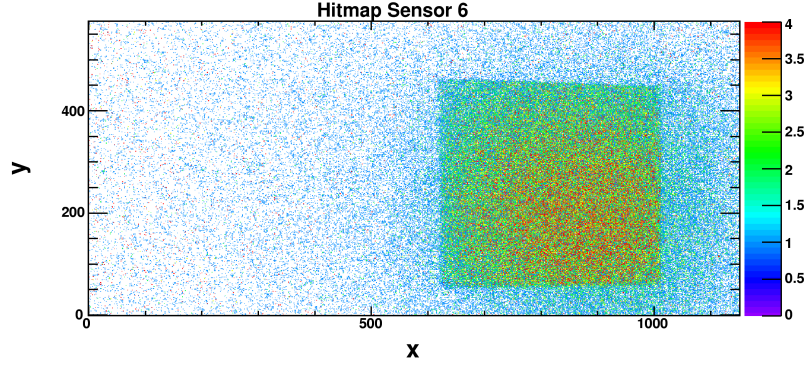
Figure 5.5: The distribution of reconstructed hits on one of the Mimosa 26 sensors.

material can be neglected and that the thickness of the material in which the particles can scatter is small compared to the distance of the individual planes.
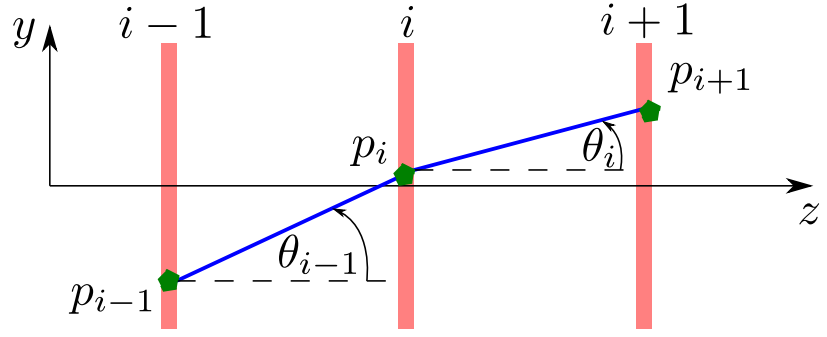
Figure 5.6: The definition of the variables θ_i and θ_{i-1} used in the track reconstruction algorithm.

The tracks are then reconstructed by minimising a χ^2 function according to

$$\Delta\chi_i^2 = \left(\frac{y_i - p_i}{\sigma_i}\right)^2 + \left(\frac{\theta_i - \theta_{i-1}}{\Delta\theta_i}\right)^2, \tag{5.1}$$

where $\Delta\chi_i^2$ is the contribution arising from plane i, y_i the measured particle position and p_i the predicted position. The angles θ_i and θ_{i-1} correspond to the angle between the nominal beam direction (the z axis) and the track direction as shown in figure 5.6. In the first and the last plane the term due to multiple scattering is omitted. The quantity $\Delta\theta_i$ is the expected width of the distribution of the scattering angle. This variable can be determined for small scattering angles [51] according to

$$\Delta\theta = \frac{13.6 \text{ MeV}}{\beta cp} \cdot z\sqrt{\frac{dx}{X_0}}\left[1 + 0.038 \cdot \ln\left(\frac{dx}{X_0}\right)\right], \tag{5.2}$$

where βc is the velocity, p the momentum, z the charge of the beam particle, X_0 the radiation length of the material and dx the thickness of the material. The analytical fitter extracts the necessary information like the radiation length from the corresponding Gear file. The quantity X_0 was set in this analysis to 9.36 cm, which is the radiation length of silicon. For inactive material only the last term in equation 5.1 contributes to the total χ^2. The track parameters are determined analytically.
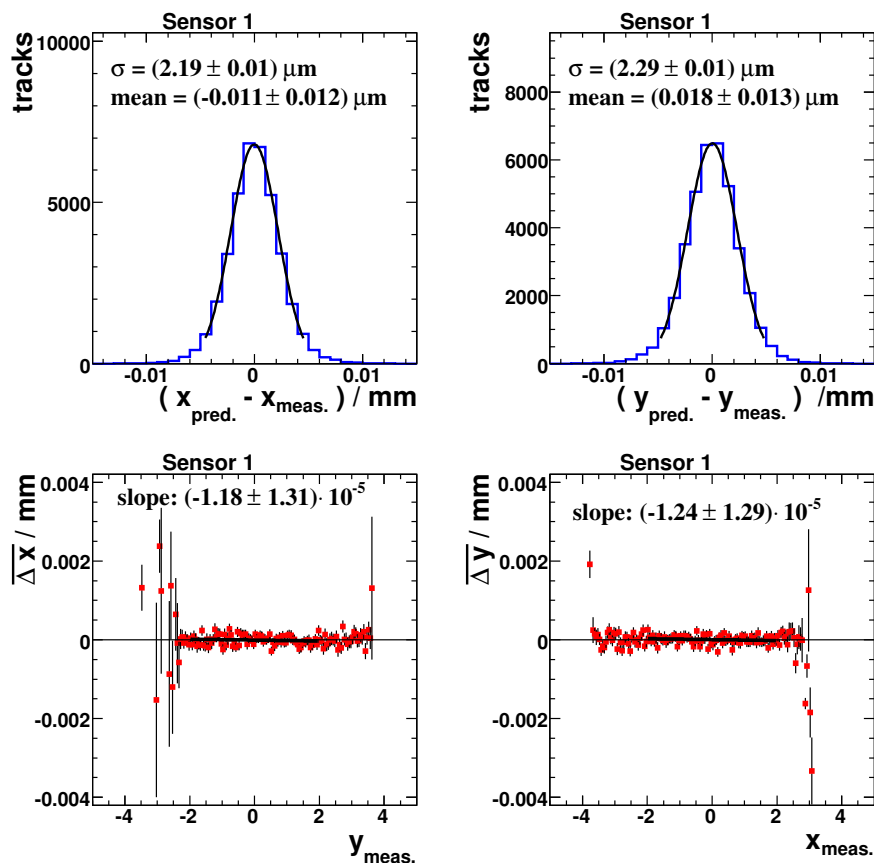
Figure 5.7: Investigation of the telescope alignment for telescope sensor 1. Shown are residual plots in x and y direction and $\overline{\Delta x}$ $(\overline{\Delta y})$ as a function of $y_{\mathrm{meas.}}$ $(x_{\mathrm{meas.}})$.

In order to investigate the alignment of the telescope sensors, a track reconstruction was performed with the requirement that only those tracks were considered with one reconstructed hit in each plane. The three Mimosa 26 sensors were treated as passive layers and not included in the fit. Afterwards, (biased) residual distributions between the coordinates of the measured hit and the predicted position for the telescope planes were determined as shown in figure 5.7 for sensor 1. Similar figures for the other telescope sensors are shown in appendix A.1. These residuals are shifted in general by less than 0.1 μm with respect to the origin. In addition, in these figures the average residual $\overline{\Delta x}$ $(\overline{\Delta y})$ as a function of y (x) is depicted. The slope of these distributions can be exploited in order to roughly estimate the misalignment related to rotations around the z axis. Therefore, straight lines were fitted to these distributions. Since the values for the slopes as extracted from the fit and the determined fit uncertainties have a comparable size, the result of the alignment procedure was reasonable.

Figures 5.8, 5.10 and 5.10 show the residual distributions and the quantity $\overline{\Delta x}$ $(\overline{\Delta y})$ as a function of y (x) for the three DUT planes. These planes were *not* included in the fit. Therefore, hits in the DUT planes were assigned to the track if the distance between the hit and the predicted hit position was smaller than 100 μm. The residual distributions were first fitted with Gaussian functions without restricting the fit range.
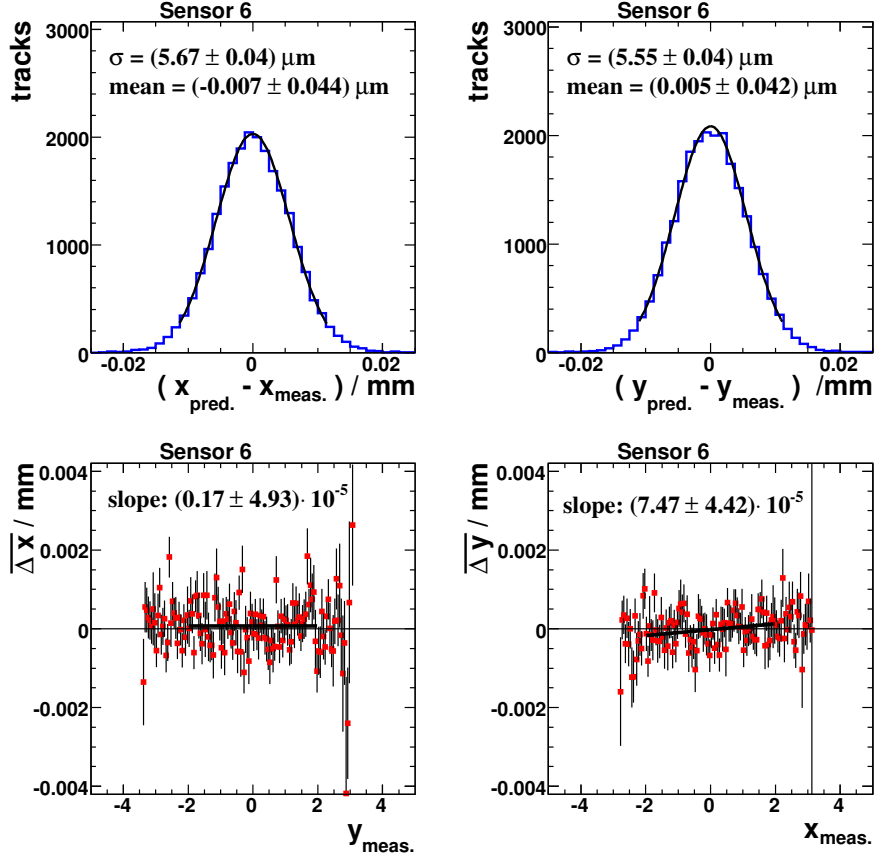
Figure 5.8: The observed residuals and the quantity $\overline{\Delta x}$ $(\overline{\Delta y})$ as a function of y (x) for the MIMOSA 26 sensor 6. The sensors was not included in the track fit.

Afterwards, the fit was repeated and restricted to the range $[-2\sigma, 2\sigma]$. The obtained values for the resolutions are depicted in the figures as well. The positions of the maxima are shifted by typically less than 0.03 μm with respect to the origin. The alignment procedure has also sufficiently accounted for rotational misalignments of the three DUT planes within the uncertainties.

The observed (measured) resolutions in the DUT planes consisted of convolutions of the reference-telescope resolution, the single-point resolution of the MIMOSA 26 sensor and the contribution from multiple scattering, which was in the analysed data samples negligible. Therefore, the MIMOSA 26 single-point resolution, σ_{M26}, can be expressed according to

$$\sigma_{\mathrm{M26}}^2 = \sigma_{\mathrm{meas.}}^2 - \sigma_{\mathrm{tel.}}^2 - \cancel{\sigma_{\mathrm{MS}}^2}, \tag{5.3}$$

where $\sigma_{\mathrm{meas.}}$ represents the measured resolution, σ_{MS} the contribution from multiple scattering and $\sigma_{\mathrm{tel.}}$ the intrinsic telescope resolution. The latter can be determined from the single-point resolution of the telescope sensors:

$$\sigma_{\mathrm{tel}}^2 = k \cdot \sigma_{\mathrm{MimoTEL}}^2 \tag{5.4}$$
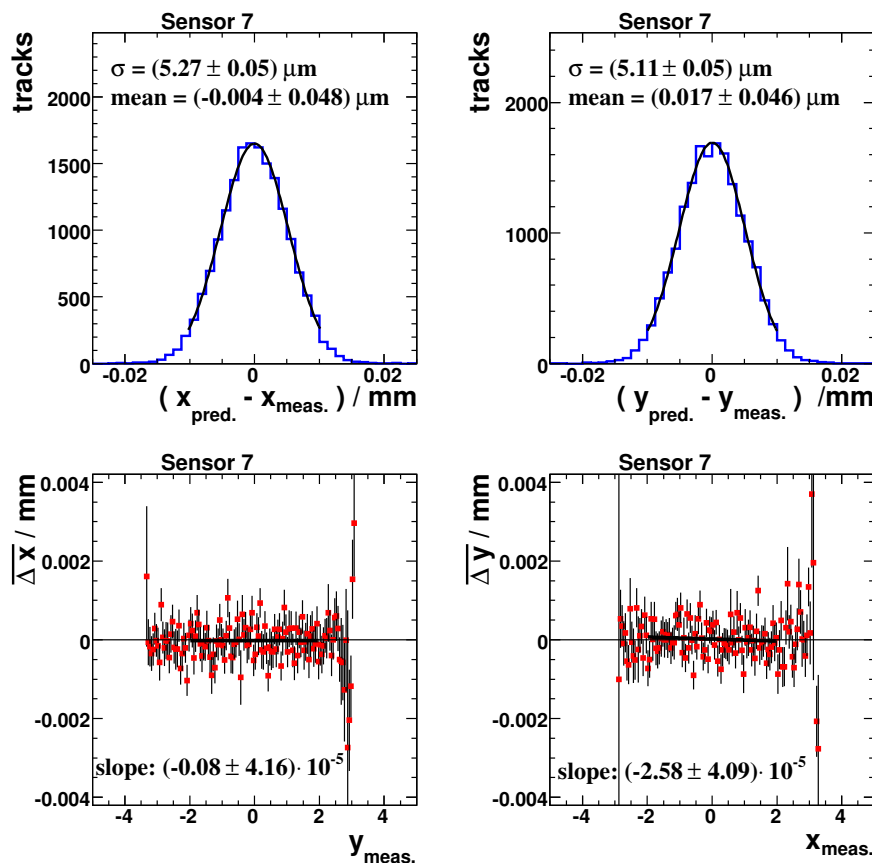
Figure 5.9: The observed residuals and the quantity $\overline{\Delta x}$ $(\overline{\Delta y})$ as a function of y (x) for the MIMOSA 26 sensor 6. The sensors was not included in the track fit.

The variable k is a geometrical scaling factor [20, 21] that can be calculated according to

$$k = \frac{\sum_i^N z_i^2}{N \sum_i^N z_i^2 - \left(\sum_i^N z_i\right)^2},$$ (5.5)

where the variable z_i is the z position of plane i under the assumption that the DUT is placed at the origin of the coordinate system, $z = 0$. In this determination the contributions from multiple scattering were neglected due to the high-energetic (120 GeV) beam particles and due to the small sensor thickness ($< 700 \ \mu$m).

With a single-point resolution of the telescope planes of $\sigma_{\text{MimoTEL}} \approx 3.5 \ \mu$m the observed resolution can be used for an extraction of the MIMOSA 26 single-point resolution as depicted in table 5.1.4. Statistical uncertainties are not given because the spread between the sensors and between the x and y direction indicates that the measurement was dominated by not-understood systematic uncertainties.

Owing to the used threshold settings most of the clusters were single-pixel cluster as shown in figure 5.11, where for clusters assigned to tracks the pixel multiplicity is depicted. The amount of single-pixel cluster has ranged from about 55% to 75%. Even though all three MIMOSA 26 sensors were configured with the same threshold
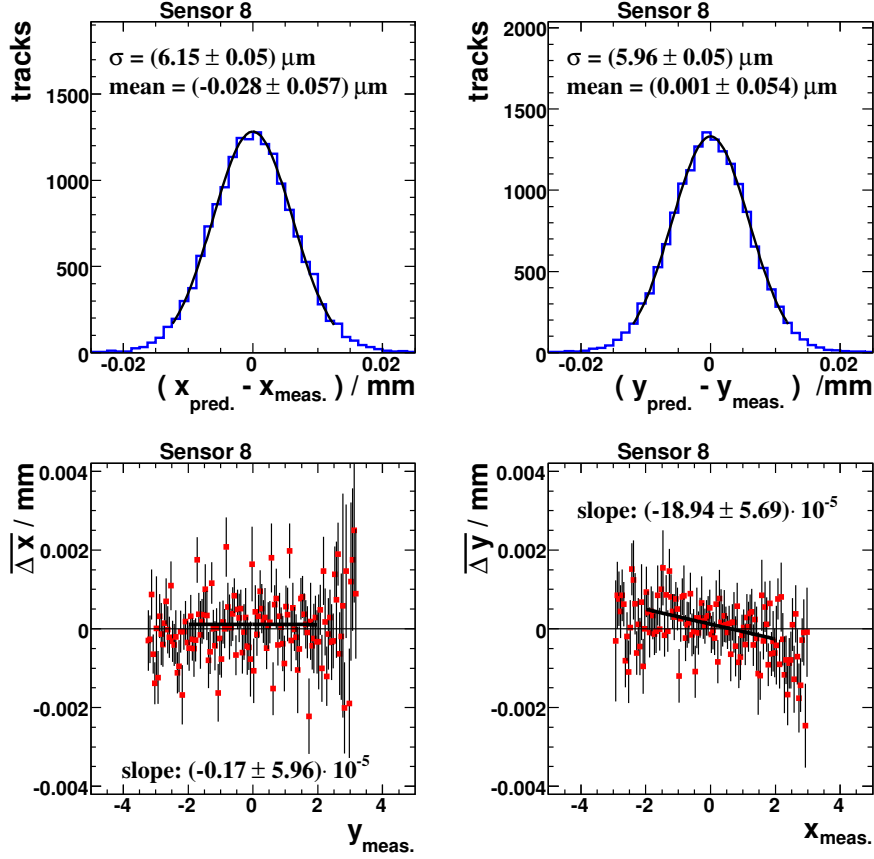
Figure 5.10: The observed residuals and the quantity $\overline{\Delta x}$ $(\overline{\Delta y})$ as a function of y (x) for the MIMOSA 26 sensor 6. The sensors was not included in the track fit.

settings, significant differences between the sensors are visible. Since these differences possibly have a large impact on the obtained results for the resolutions, a deeper understanding of this effect is mandatory for a more precise extraction of the resolution. A further possible improvement would be the consideration of multiple scattering.

For a data sample that consists of single-pixel clusters only, the resolution can be calculated according to [16]

$$\sigma_{\text{dig}} = \frac{P}{\sqrt{12}} = \frac{18.4 \ \mu\text{m}}{\sqrt{12}} = 5.31 \ \mu\text{m}, \tag{5.6}$$

where P represents the pixel pitch, which is 18.4 μm for MIMOSA 26. Since the investigated data were dominated by single-pixel cluster the extracted resolutions are roughly similar to σ_{dig}.

During the analysis of the data it was observed that part of the data were affected by a jitter of the x coordinate[2] of the clusters. During one run it occasionally happened that the x coordinates of all pixel in the data stream were shifted by exactly one pixel pitch. This effect was observed in the data of all three MIMOSA 26 sensors simultaneously.

---

[2]The y coordinate was not affected.

32

Table 5.1: The single-point resolutions and the geometrical scaling factor, k, for the three Mimosa 26 sensors determined with a signal-to-noise threshold of $S/N > 12$.

Sensor ID	σ_x	σ_y	k
Sensor 6	5.48 μm	5.35 μm	0.174
Sensor 7	5.07 μm	4.90 μm	0.169
Sensor 8	5.98 μm	5.78 μm	0.168

In order to illustrate this effect, figure 5.12 shows the residual distribution in the x direction in one of the Mimosa 26 sensors. A distinct second peak with exactly one pixel pitch distance is visible. Later after the data-taking it was found that the shielding of the electrical cables connected to the sensors was insufficient resulting in unpredictable and unstable behaviour of the whole data-acquisition system [29]. Possibly this could have caused the observed jitter. Therefore, it was decided to restrict the analysis to the part of the data where this effect was not observed.

5.2. September 2009 Test Beam

During the September 2009 test beam the sensors of the telescope were upgraded to six Mimosa 26 sensors of which five could be used. A signal-to-noise threshold of $S/N > 10$ was applied to the Mimosa 26 sensors. In this section the results of the data analysis are presented.

The data taken during the September 2009 test beam were affected by two TLU problems: 1) From time to time the synchronisation between the two VME crates was lost. 2) Since the read trigger numbers were always equal to zero, this synchronisation problem could not be fixed offline.

In order to recover at least part of the data, the spatial correlation between the cluster positions in neighbouring planes was investigated. Therefore, the data were chopped into several small sets and for each set the cluster correlations were investigated. Only those data that have exhibited a clear correlation were further analysed. Additionally, the data set that was taken directly before the first set without visible correlation was also removed from the analysis. Owing to this procedure about 200000 out of 1.5 million events could be recovered and analysed.

The track reconstruction was performed as described in the previous section by using four of the five available sensor planes. The hits in the sensor plane not used in the track fit were assigned to the track if the distance between the predicted track position and the hit position was smaller than 100 μm. Figures 5.13 and 5.14 present the extracted residual distributions for each sensor plane separately. For each distribution the corresponding sensor plane was removed from the track reconstruction. These distributions were fitted with Gaussian functions and the resolution, $\sigma_{\text{meas.}}$, was extracted as described in the previous section. Since the measured resolutions for the x and y direction differ significantly, a systematic uncertainty of 0.10 μm estimated from the spread was assigned to the extracted resolutions. Therefore, this systematic uncertainty was considered in the extraction of the single-point resolution of the Mimosa 26 sensor. Different resolutions for the x and y direction were also observed in previous analyses [52].
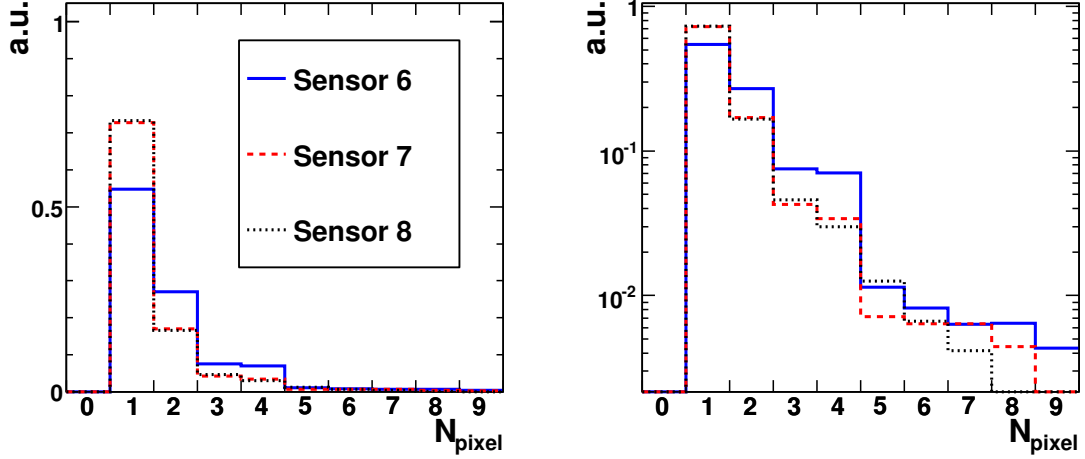
Figure 5.11: Pixel multiplicity per cluster for the three Mimosa 26 sensors.

The prediction for the measured resolution can be calculated from the single-point resolution of the Mimosa 26 sensor, σ_{M26}, and the geometrical scaling factor, k, according to

$$\sigma_{\text{meas.}}^2 = \sigma_{\text{M26}}^2 + \sigma_{\text{tel.}}^2 + \cancel{\sigma_{\text{MS}}^2}, \tag{5.7}$$

and

$$\sigma_{\text{tel}}^2 = k \cdot \sigma_{\text{M26}}^2, \tag{5.8}$$

under the assumption that all telescope sensors have the same single-point resolution and that $\sigma_{\text{MS}} = 0$.

Figure 5.15 shows the prediction for the measured resolution, $\sigma_{\text{meas.}}$, as a function of the z coordinate for different values of σ_{M26} in comparison with the measured values extracted from the residual distributions shown in figures 5.13 and 5.14. The combined single-point resolution of the Mimosa 26 sensors was extracted from that figure with a χ^2 minimisation method ($\chi^2/\text{ndf} \approx 1.2$). The extracted value for the single-point resolution was determined to be $\sigma_{\text{M26}} = [4.35 \pm 0.10\,(sys)]\ \mu\text{m}$ and is indicated in the figure as a filled band. Within the systematic uncertainties the agreement between the measurement and the prediction of its dependence on the sensor position is reasonable. The quality of the track reconstruction is illustrated in figure 5.16 where the distribution of the quantity χ^2 of the tracks is shown. The data are compared with the expected χ^2 distribution [53] for four degrees of freedom[3]. The expected χ^2 distribution agrees with the data reasonably well. The obtained single-point resolution for the applied threshold setting agrees within the uncertainties with the results from the Mimosa 26 developers [22, 23] with a tendency towards

---

[3]In total four planes with 8 measurements were used in the track reconstruction. The number of fitted parameters was equal to 10 and the number of used constrains on multiple scattering was 6 (three inner sensor planes).
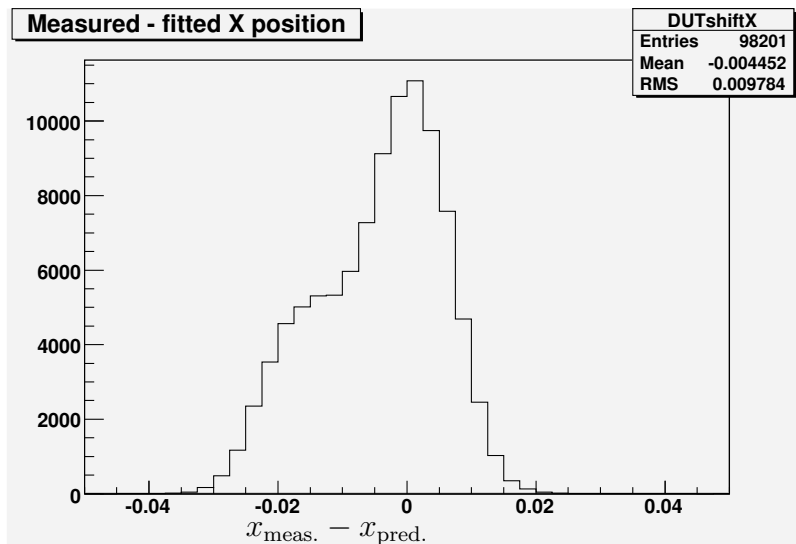
Figure 5.12: The Residual distribution in x direction for one Mimosa 26 sensor.

smaller values. Since multiple scattering was neglected, a possibly slightly smaller single-point resolution can be extracted by taking this effect into account.

The extracted single-point resolution can be utilised to calculate the intrinsic telescope resolution for the employed threshold setting and the used geometrical setup. For the investigated setup with four planes used in the track reconstruction and with a signal-to-noise threshold of $S/N > 10$ the intrinsic telescope resolution in the central sensor plane was determined to be (2.22 ± 0.05) μm. This resolution can significantly be improved by performing the track reconstruction with six planes instead of four and by applying a lower threshold setting during the data taking. For a telescope setup (threshold $S/N > 10$) with six planes where the distance between neighbouring planes is equal to 10 cm, an intrinsic telescope resolution of $1.9 - 2.0$ μm in the DUT layer centered between the two arms can be reached.

In addition to the determination of the resolution, the detection efficiency of the central sensor plane (sensor 2) was investigated. The efficiency was determined with the ratio of number of hits assigned to tracks over the total number of predicted hits. Measured hits were assigned to tracks if the distance between the measured and predicted hit position was smaller than 100 μm. Figure 5.17 shows the efficiency in x and y direction, fake hit rate and the predicted track positions. The fake hit rate was determined by using for the central sensor plane data from the previous event. These hits were assigned to the track if the distance was smaller than 100 μm. This rate was in general between 10^{-4} and 10^{-3} and, therefore, significantly larger than the expectation of 10^{-5} [23]. The reason could be that during the data taking a larger amount of electronic noise in the system than expected was observed. The dip at $x \approx -5$ mm in the plot that shows the predicted track positions is caused by sensor 0, because the dip disappears after removing sensor 0 from the track reconstruction. After the test beam campaign it was found that the JTAG programming of sensor 0 was insufficient [29] which could have caused such a behaviour.

The detection efficiency for the signal-to-noise threshold $S/N > 10$ was determined to be approximately $\approx 95.5\%$ in the region of the trigger window, which is larger than the expectation [22, 23] of 94%. The location of the trigger window is clearly visible

in the efficiency histogram.

One possible explanation [29, 54] that could explain the different efficiencies in the region of the trigger window and outside this window can be the following: As a consequence of the rolling-shutter mode, each pixel contains the signals that correspond to a time which is equal to the integration time of the sensors ($\approx 110 \ \mu$s). Hence, the effective sensitive time window for each pixel is shifted relative to the others. Moreover, in the offline analysis during conversion two frames are combined such that the data from the current frame is taken up to the pivot row. The remaining parts are taken from the previous frame. Those parts taken are called in the following "active" and the discarded parts "inactive". For particles passing the detector in coincidence with the trigger signal the whole sensor matrix is "active". The relative fraction of the "inactive" area increases the more the particles moves in time away from the trigger signal. Since the sensors read-out by EUDRBs in one VME crate are read-out synchronously, the pixel address in pixel units is for those sensors identical (typically in the range ± 1 pixel units). However, relative transverse shifts of the sensors result in different geometrical pivot row positions in the (x, y)-coordinate system. Hence, particles passing one sensor in the "active" part of the matrix can possibly pass the other sensors in the "inactive" parts. Due to the fact that the relative fraction of the "active" area is for out-of-time particles much smaller than for particles passing in coincidence with the trigger signal the sensors, the efficiency for the detection of out-of-time hits is slightly smaller. The same behaviour should not only occur for small shifts but also for tracks with an angle with respect to the z axis and for a tilted/rotated telescope.

Since the average track multiplicity per event is about ≈ 1.2 and the efficiency difference between particles in the region of the trigger window and out-of-time particles is about $\sim 4\%$, the contributions from out-of-time particles to the measured efficiency in the region of the trigger window, where the observed efficiency is a weighted average, amounts to approximately $\approx 1\%$.
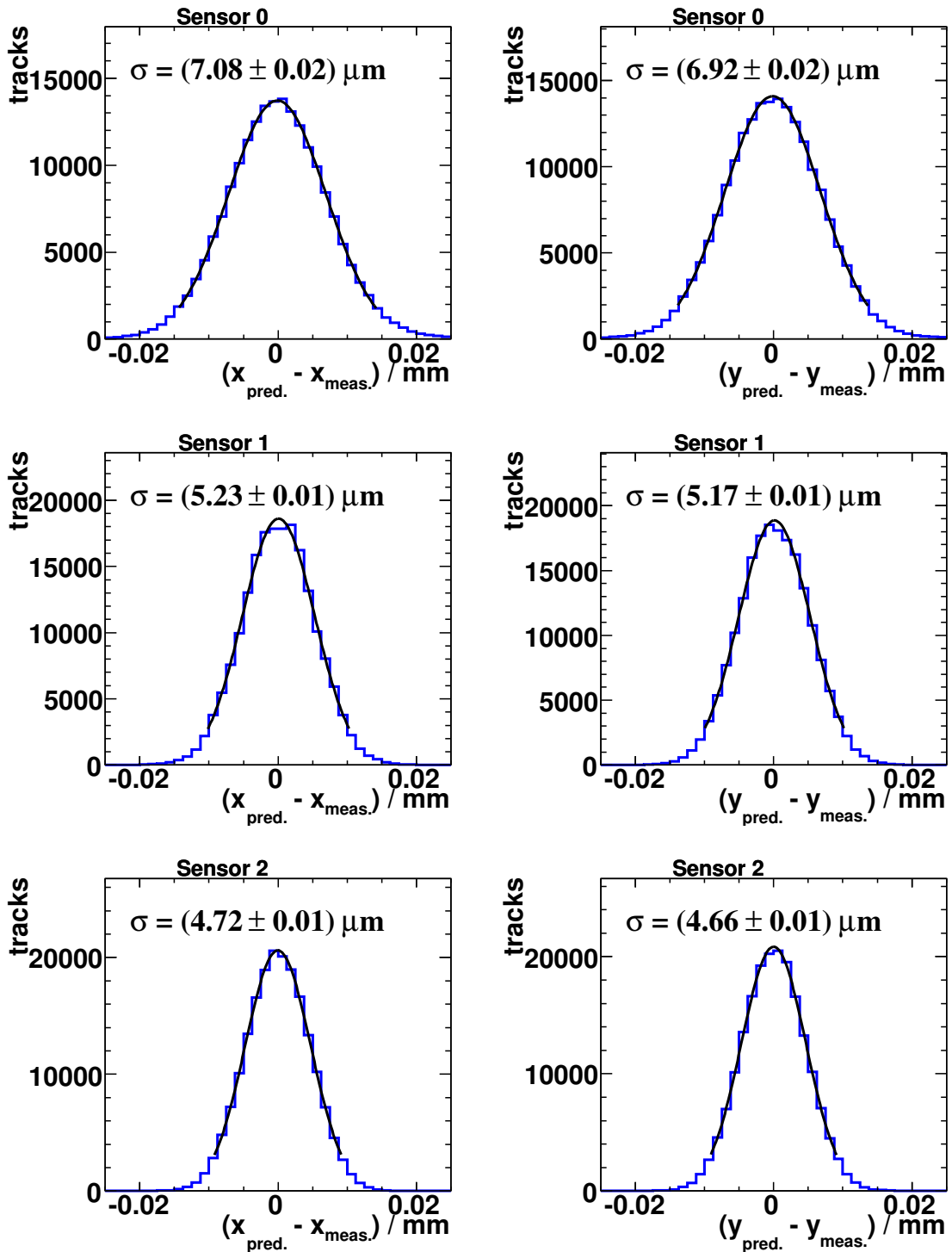
Figure 5.13: Residual distributions in x and y direction for the September 2009 data. The corresponding sensors were treated as passive layers in the track reconstruction.
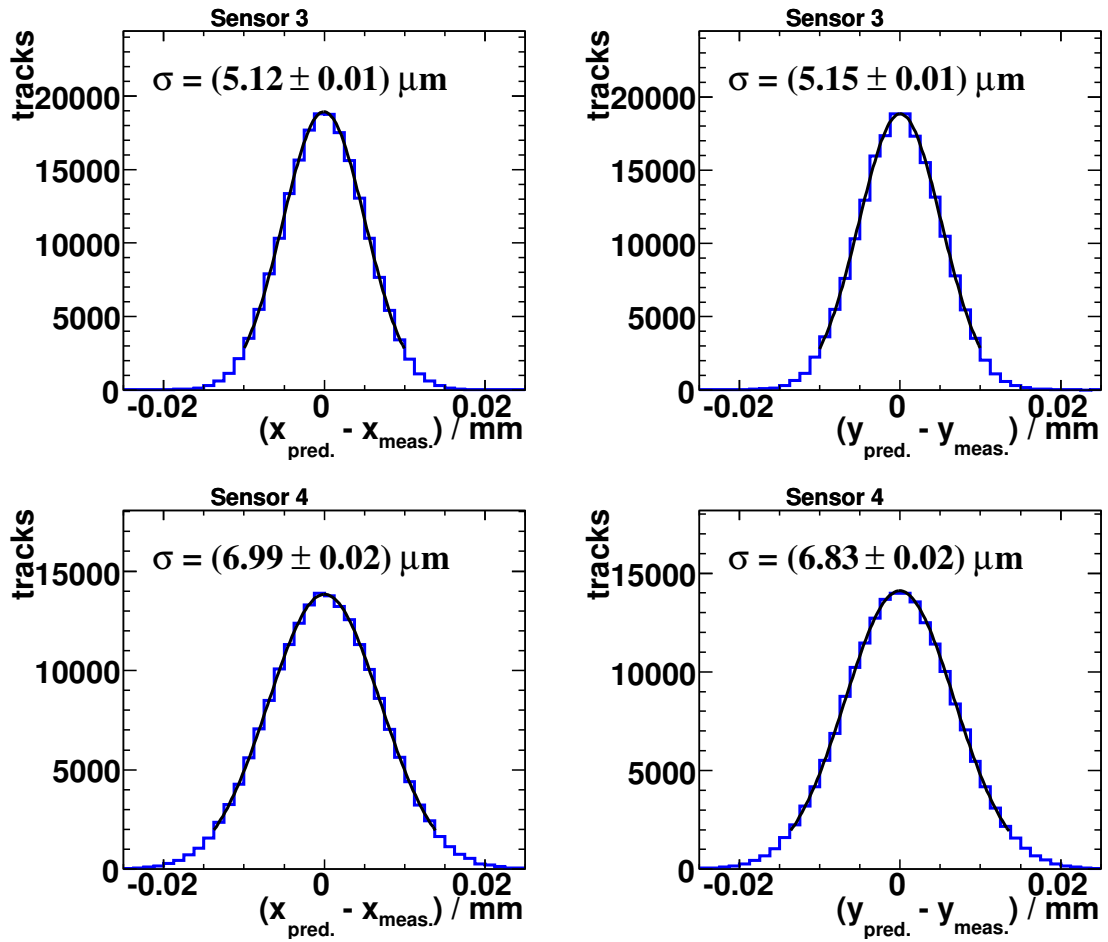
Figure 5.14: Residual distributions in x and y direction for the September 2009 data. The corresponding sensors were treated as passive layers in the track reconstruction.
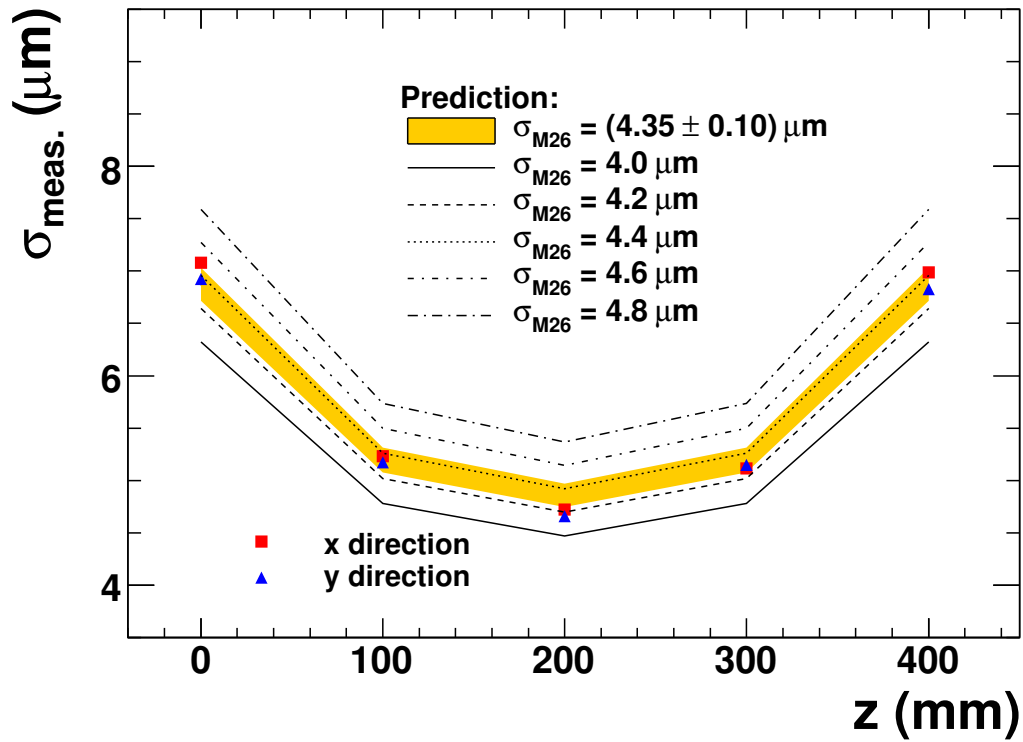
Figure 5.15: The measured resolution, $\sigma_{\mathrm{meas.}}$, as a function of the z coordinate. The corresponding sensor plane for each data point was treated as passive layer in the track reconstruction.
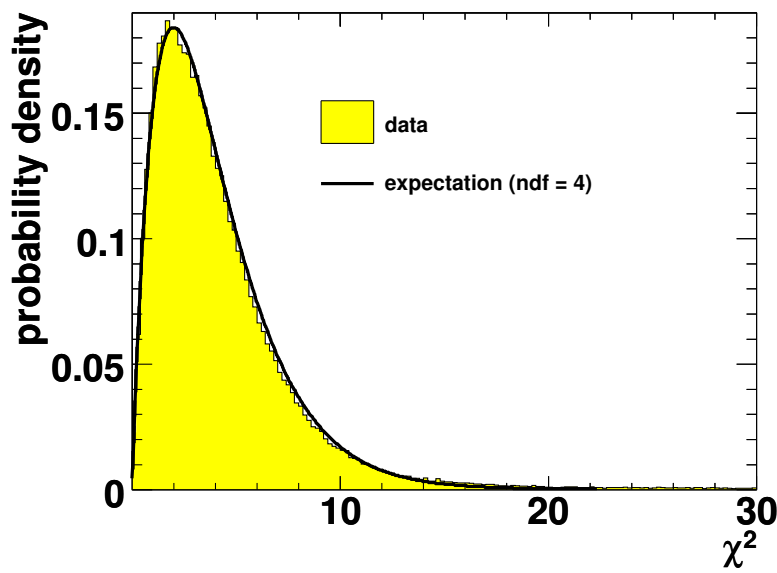

Figure 5.16: Distribution of the quantity χ^2 for reconstructed tracks in comparison with the expectation for four degrees of freedom (ndf).
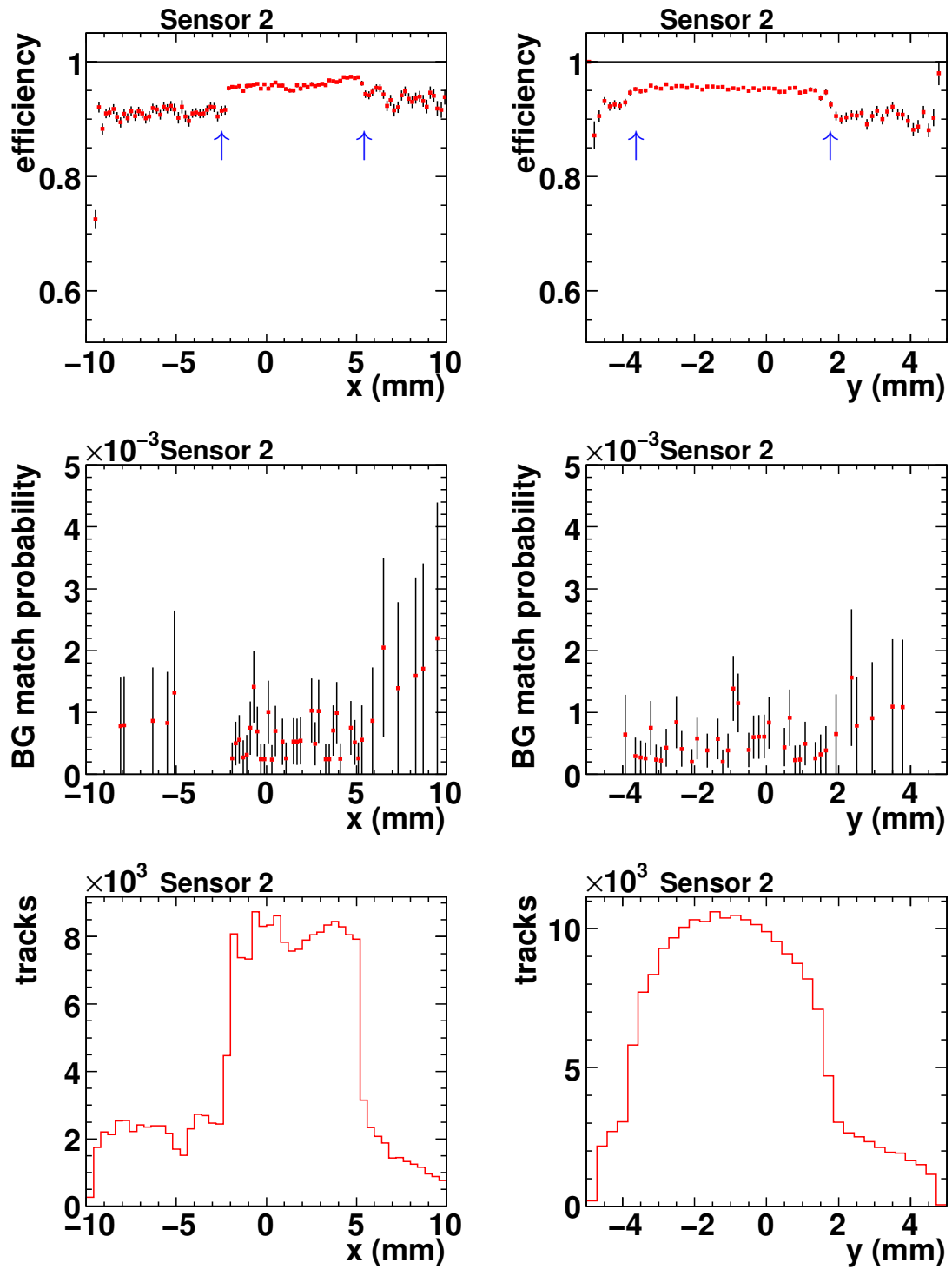
Figure 5.17: The detection efficiency in x and y direction, the probability to match background (BG) hits to the reconstructed track and the predicted track positions in the sensor plane. In the efficiency plots the position of the trigger window is indicated with small arrows.

6. Summary and Conclusion

The EUDET high-resolution test-beam telescope was designed to be used in a wide range of detector research and development studies. The provided infrastructure is flexible and portable in order to allow the investigation of rather different devices-under-test. The telescope can be used at high-energy hadron beams (e.g. > 100 GeV at the SPS facility at CERN) as well as at low-energetic electron beams ($1 - 6$ GeV at DESY). The telescope consists of two arms each equipped with three pixel sensors; the device-under-test can be installed for instance between the two arms.

In the EUDET project a two stage approach for the construction of the telescope was chosen: First, the so-called "demonstrator telescope" was constructed equipped with well established analog sensors (MimoTEL). Afterwards, the telescope was upgraded in Summer 2009 to sensors with binary output (Mimosa 26) in order to match the design requirements – in particular to reach a higher readout rate of about 1 kHz.

In this thesis, the usability, flexibility and performance of the online-monitoring system was improved by introducing new histograms, adjusting the reconstruction algorithms and by implementing new elements into the graphical user interface. Additionally, the offline-analysis software was adapted to cope with the new binary Mimosa 26 sensors installed in the final telescope.

The very first analysis of two different data samples taken with these new sensors in the EUDET telescope was presented:

- First, a data sample was analysed in which the "demonstrator telescope" was used as a reference system. Three Mimosa 26 were installed as devices-under-test. These devices-under-test were configured with signal-to-noise thresholds of $S/N > 12$ resulting in a data sample dominated by single-pixel clusters. The offline analysis software was successfully adapted to the new requirements of binary sensors. For the applied threshold setting a Mimosa 26 single-point resolution of about 5.3 μm was determined.

- The second analysed data sample consisted of data taken with the final telescope upgraded to six Mimosa 26 sensors, of which five could be used. The applied threshold setting was $S/N > 10$ in order to improve the resolution and detection efficiency. The measured residual widths were found to be consistent with a single-point resolution of $\sigma_{\mathrm{M26}} = [4.35 \pm 0.10\,(sys)]$ μm. Therefore, a telescope equipped with six sensors can reach an intrinsic telescope resolution in the order of $1.9 - 2.0$ μm for a threshold of $S/N > 10$. The detection efficiency was determined to be approximately 95%, while the fake rate was found to be below 10^{-3}.

The EUDET telescope was upgraded successfully to the final version over the Summer 2009. Since then it was successfully used by several different groups and it will extensively be utilised in the future.

Acknowledgement
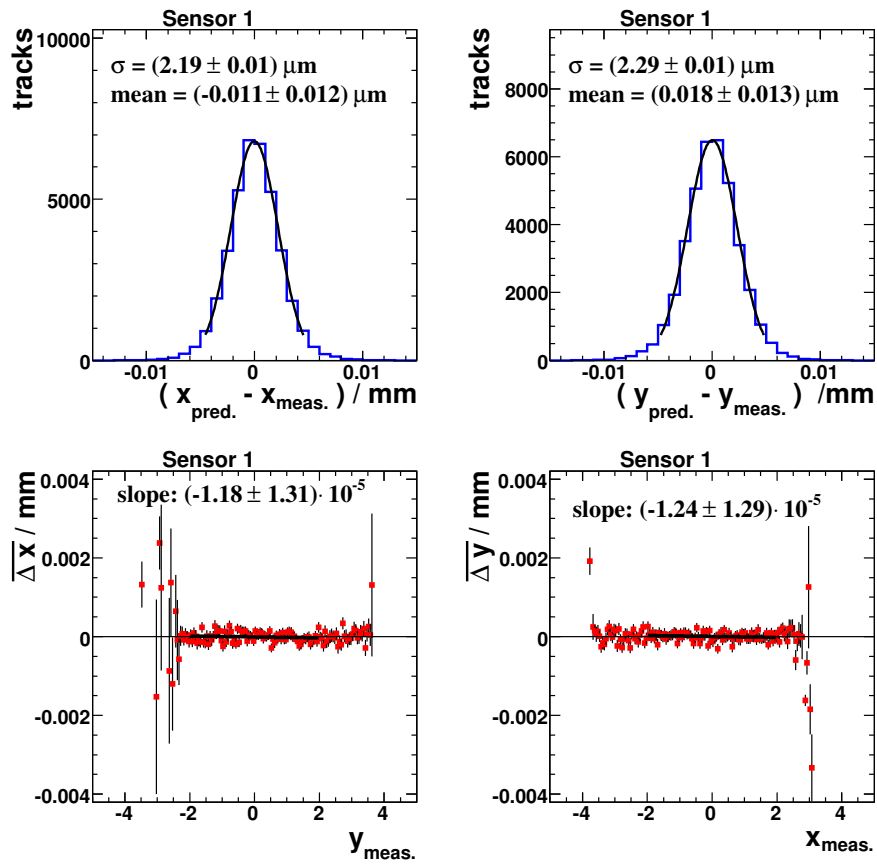
A. Appendix

A.1. Pixel Telescope

Figure A.1: Investigation of the telescope alignment for sensor 1. Shown are residual plots in x and y direction and $\overline{\Delta x}$ ($\overline{\Delta y}$) as a function of $y_{\text{meas.}}$ ($x_{\text{meas.}}$).

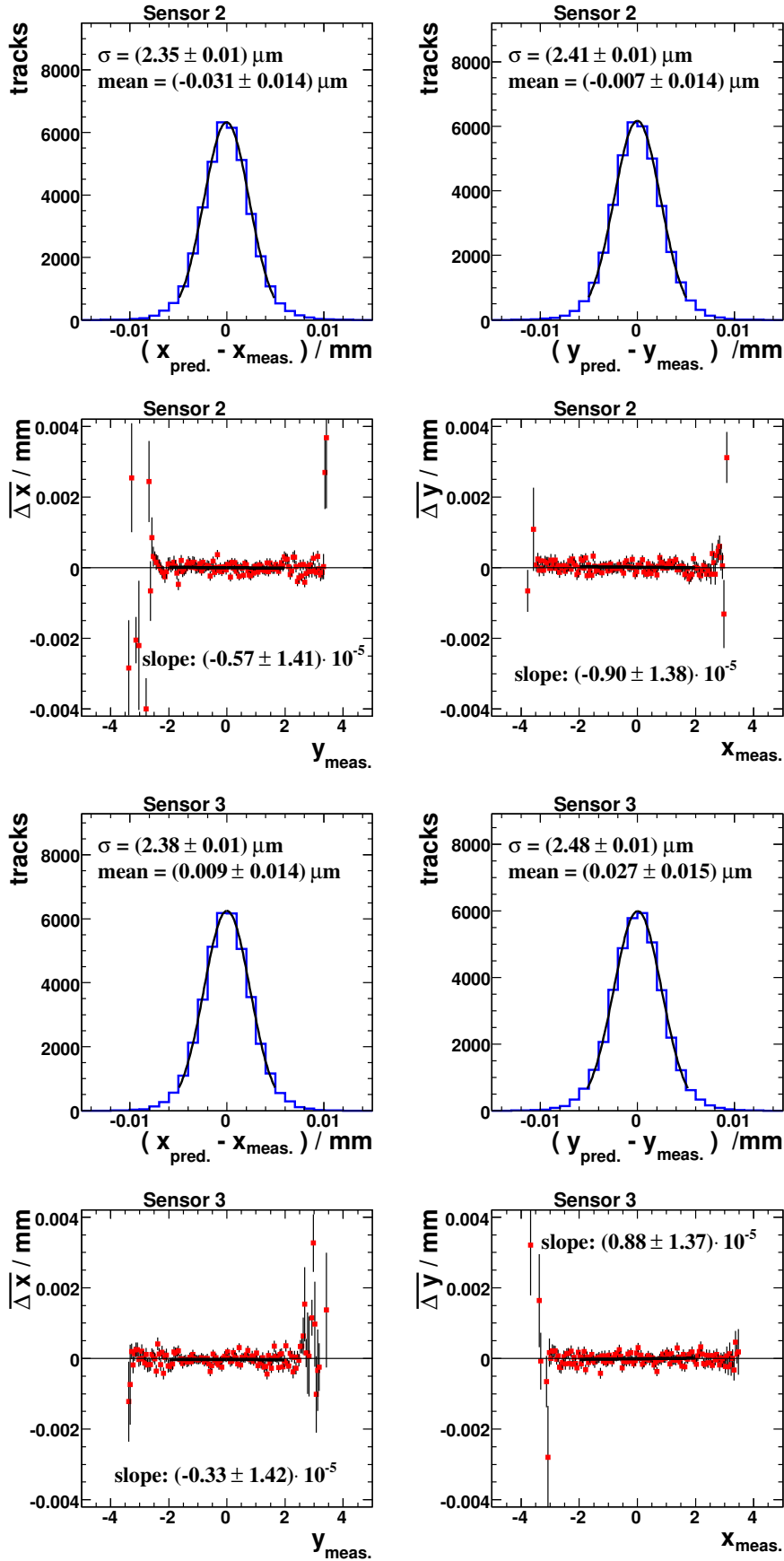**Figure A.2**: Investigation of the telescope alignment for the sensors 2 and 3. Shown are residual plots in x and y direction and $\overline{\Delta x}$ ($\overline{\Delta y}$) as a function of $y_{\mathrm{meas.}}$ ($x_{\mathrm{meas.}}$).
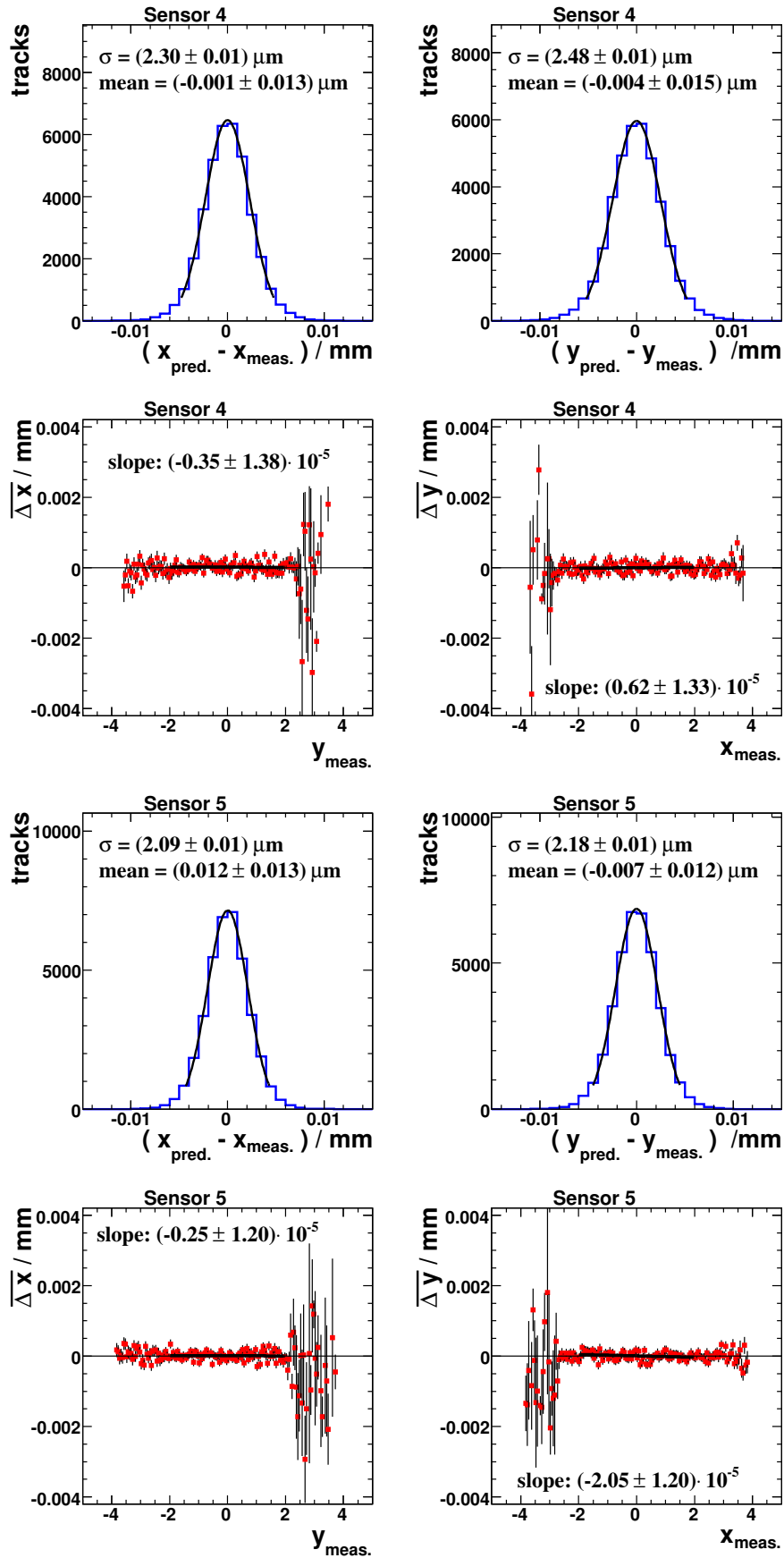
Figure A.3: Investigation of the telescope alignment for the sensors 4 and 5. Shown are residual plots in x and y direction and $\overline{\Delta x}$ ($\overline{\Delta y}$) as a function of $y_{\mathrm{meas.}}$ ($x_{\mathrm{meas.}}$).

Bibliography

[1] James Brau, (Ed.) et al. ILC Reference Design Report Volume 1 - Executive Summary. 2007.

[2] R. Tomás. Overview of the Compact Linear Collider. *Phys. Rev. ST Accel. Beams*, 13(1):014801, Jan 2010. doi:10.1103/PhysRevSTAB.13.014801.

[3] Marco Battaglia. Physics case and challenges for the vertex tracker at future high-energy e^+e^- linear colliders. *Nucl. Instrum. Meth.*, A473:75–78, 2001. doi:10.1016/S0168-9002(01)01123-8.

[4] Gerald Aarons et al. International Linear Collider Reference Design Report Volume 2: PHYSICS AT THE ILC. 2007.

[5] Ties Behnke, (Ed.) et al. ILC Reference Design Report Volume 4 - Detectors. 2007.

[6] T. Behnke, (ed.), S. Bertolucci, (ed.), R. D. Heuer, (ed.), and R. Settles, (ed.). TESLA: The superconducting electron positron linear collider with an integrated X-ray laser laboratory. Technical design report. Pt. 4: A detector for TESLA. 2001. DESY-01-011.

[7] K. D. Stefanov. CCD vertex detector for the future linear collider. *Nucl. Instrum. Meth.*, A501:245–250, 2003. doi:10.1016/S0168-9002(02)02042-9.

[8] R. Turchetta et al. A monolithic active pixel sensor for charged particle tracking and imaging using standard VLSI CMOS technology. *Nucl. Instrum. Meth.*, A458:677–689, 2001. doi:10.1016/S0168-9002(00)00893-7.

[9] Yu. Gornushkin et al. Tracking performance and radiation tolerance of monolithic active pixel sensors. *Nuclear Instruments and Methods in Physics Research Section A*, 513(1-2):291 – 295, 2003. ISSN 0168-9002. doi:10.1016/j.nima.2003.08.050. Proceedings of the 6th International Conference on Position-Sensitive Detectors.

[10] P. Fischer, W. Neeser, M. Trimpl, J. Ulrici, and N. Wermes. Readout concepts for DEPFET pixel arrays. *Nucl. Instrum. Meth.*, A512:318–325, 2003. doi:10.1016/S0168-9002(03)01909-0.

[11] I. Gregor and C. Muhl. JRA1 - Status of Machanics, Cooling and Infrastructure. EUDET-Memo-2007-26, 2007.

[12] I. Peric, Ch. Takacs, J. Behr, and P. Fischer. The first beam test of a monolithic particle pixel detector in high-voltage CMOSTechnology. In *12th Vienna Conference for Instrumentation VCI2010*. proceedings submitted to Elsevier, 2010.

[13] C. Takacs. TEST SYSTEM SETUP AND EVALUATION OF TESTBEAM MEASUREMENTS OF A NOVEL MONOLITHIC PIXEL PARTICLE DETECTOR IMPLEMENTED IN HIGH VOLTAGE TECHNOLOGY. Diploma thesis, Ruprecht-Karls-Universität Heidelberg, 2009.

[14] The EUDET JRA1 Group. JRA1 Delivery: Test Report on EUDET High Resolution Pixel Telescope. EUDET-Report-2008-04, 2008.

[15] Bart Dierickx, Guy Meynants, and Danny Scheffer. Near-100 % fill factor standard CMOS active pixel. In *IEEE Workshop on Charge-Coupled Devices & Advanced Image Sensors*, 1997.

[16] L. Rossi, P. Fischer, T. Rohe, and N. Wermes. *Pixel detectors: From fundamentals to applications*. Springer, 2006. Berlin, Germany.

[17] M. Deveaux et al. Radiation Tolerance of CMOS Monolithic Active Pixel Sensors with Self-Biased Pixels. *ArXiv e-prints*, August 2009. URL http://adsabs.harvard.edu/abs/2009arXiv0908.4202D.

[18] A. Dorokhov. Optimization of amplifiers for Monolithic Active Pixel Sensors. In S. Claude, editor, *Proc. of the Topical Workshop on Electronics for Particle Physics (TWEPP 07)*, page 423, Prague, Czech Republic, 2007.

[19] W. Dulinski. Status of pixel sensors for the demonstrator phase of the EUDET beam telescope. EUDET-Memo-2007-45, 2007.

[20] P. Niezurawski A.F. Zarnecki. EUDET Telescope Geometry and Resolution Studies. EUDET-Report-2007-01, 2007.

[21] A. Bulgheroni. Results from the EUDET telescope with high resolution planes. EUDET-Report-2009-02, 2009.

[22] M. Gelin et al. Test Results of the Zero Suppressed Digital Chip sensor for EUDET-JRA1 beam telescope. EUDET-Memo-2009-26, 2009.

[23] J. Baudot et al. JRA-1 Milestone: Validation of the Final Sensor Equipping the EUDET Beam Telescope. EUDET-Memo-2009-25, 2009.

[24] G. Claus et al. JRA1 Milestone IDC Prototype ready. EUDET-Memo-2008-03, 2008.

[25] A Himmi, A Doziere, O Torheim, C Hu-Guo, and A Winter. A Zero Suppression Micro-Circuit for Binary Readout CMOS Monolithic Sensors. *TWEPP-09: Topical Workshop on Electronics for Particle Physics, Paris, France*, pages 426–430, 2009.

[26] J. Baudot. First Test Results of MIMOSA-26, a Fast CMOS Sensor With Integrated Zero Suppression and Digitized Output. IEEE Nuclear Science Symposium, 2009.

[27] A. Cotta Ramusino. The EUDET Data Reduction Board (EUDRB). EUDET-Memo-2007-36, 2007.

[28] A. Cotta Ramusino. The EUDET Data Reduction Board (EUDRB). EUDET-Memo-2008-38, 2008.

[29] Ingrid-Maria Gregor. private communication.

[30] D Cussans. A Trigger/Timing Logic Unit for ILC Test-beams. *Topical Workshop on Electronics for Particle Physics, Prague, Czech Republic*, pages 420–422, 2007.

[31] D. Cussans. Description of the JRA1 Trigger Logic Unit (TLU). EUDET-Memo-2007-02, 2007.

[32] D. Cussans. Progress on the JRA1 Trigger Logic Unit (TLU). EUDET-Memo-2007-46, 2007.

[33] D. Cussans. Description of the JRA1 Trigger Logic Unit (TLU), v0.2c. EUDET-Memo-2009-04, 2009.

[34] D. Cussans. Status of the TLU v0.2. EUDET-Memo-2009-29, 2009.

[35] M. Pohl D. Haas, E. Corrin. JRA1 - Data acquisition system. EUDET-Memo-2006-07, 2006.

[36] D. Haas. The DAQ for the EUDET pixel telescope. 2007. In the Proceedings of 2007 International Linear Collider Workshop (LCWS07 and ILC07), Hamburg, Germany.

[37] E. Corrin. EUDAQ Software User Manual. EUDET-Memo-2010-01, 2010.

[38] R. Brun and F. Rademakers. ROOT: An object oriented data analysis framework. *Nucl. Instrum. Meth.*, A389:81–86, 1997. doi:10.1016/S0168-9002(97)00048-X.

[39] Daniel Haas. The EUDET High Resolution Pixel Telescope – Towards the Final Telescope. EUDET-Report-2008-02, 2008.

[40] L. Reuen J. Furletova. JRA1 - The DEPFET sensor as the first fully integrated DUT in the EUDET pixel telescope: The SPS test beam 2008. EUDET-Memo-2008-34, 2008.

[41] A. Bulgheroni et al. Eutelescope: tracking software. EUDET-Memo-2007-20, 2007.

[42] A. Bulgheroni et al. EuTelescope, the JRA1 tracking and reconstruction software: a status report (Milestone). EUDET-Memo-2008-48, 2008.

[43] F. Gaede. Marlin and LCCD: Software tools for the ILC. *Nucl. Instrum. Meth.*, A559:177–180, 2006. doi:10.1016/j.nima.2005.11.138.

[44] Marlin. URL http://ilcsoft.desy.de/portal/software_packages/marlin/.

[45] J. Engels F. Gaende. Marlin et al - A Software Framework for ILC detector R&D. EUDET-Report-2007-11, 2007.

[46] Frank Gaede, Ties Behnke, Norman Graf, and Tony Johnson. LCIO: A persistency framework for linear collider simulation studies. 2003.

[47] LCIO. URL http://lcio.desy.de/.

[48] Gear – A geometry description toolkit for ILC reconstruction software. URL http://ilcsoft.desy.de/portal/software_packages/gear.

[49] Volker Blobel and C Kleinwort. A New Method for the High-Precision Alignment of Track Detectors. *DESY-02-077.*, page 10 p, Aug 2002.

[50] Volker Blobel. Millepede. URL http://www.desy.de/~blobel.

[51] Gerald R. Lynch and Orin I. Dahl. Approximations to multiple Coulomb scattering. *Nucl. Instrum. Meth.*, B58:6–10, 1991. doi:10.1016/0168-583X(91)95671-Y.

[52] A. Bulgheroni. First test beam results from the EUDET pixel telescope. In *Nuclear Science Symposium Conference Record, 2007. NSS '07. IEEE*, volume 3, pages 1878 –1884, oct. 2007. doi:10.1109/NSSMIC.2007.4436523.

[53] Bronstein, Semendjajew, Musiol, and Mühlig. *Taschenbuch der Mathematik*, page 785. Verlag Harri Deutsch, 6. edition, 2005.

[54] Emlyn Corrin. private communication.